Johnstone, S. A., & Colgan, J. P. (2018). Interpretation of low-temperature thermochronometer ages from tilted normal fault blocks. *Tectonics*, 37. https://doi.org/10.1029/2018TC005207

Interpretation of low-temperature thermochronometer ages from tilted normal fault blocks

S.A. Johnstone[1], J.P. Colgan[2]

[1] ORCID: 0000-0002-3945-2499, Geology, Geophysics, and Geochemistry Science Center, U.S. Geological Survey, Denver, CO

[2]ORCID: 0000-0001-6671-1436, Geology and Environmental Change Science Center, U.S. Geological Survey, Denver CO

Corresponding author: Samuel A. Johnstone (sjohnstone@usgs.gov)

Key Points:

- Curved particle trajectories in tilted normal fault blocks complicate the interpretation of thermochronometer ages.
- Simple interpretation of age vs. structural depth plots can significantly mis-predict the onset and rate of faulting.
- Two examples from the Basin and Range province of Nevada reveal promise for quantitative inference of slip history from kinematic descriptions of sample paths.

Abstract

Low-temperature thermochronometry is a widely-used tool for dating the timing and rate of slip on normal faults. Rates are often derived from suites of footwall thermochronometer samples, but simple 2D regression of age vs. structural depth fails to account for the fact that rocks collected at similar elevations today experienced curved particle trajectories and variable velocities during fault slip. We present a simple formulation of the thermal evolution of a rotating fault block driven by a constant extension rate to demonstrate that in these settings the regression of age-depth data is susceptible to significant errors (>10%) in the identification of the initiation and rate of faulting. We show that advection of heat and perturbation of geothermal gradients by topography influence the thermal histories of exhumed particles, but for a range of geologically reasonable fault geometries and rates these effects produce AHe ages comparable to (within ~10%) those derived from exhumation through fixed isotherms. We apply the fixed-isotherm model to published data from the Pine Forest Range, Nevada and the East Range, Nevada, by incorporating field and thermochronologic constraints into a Markov chain Monte Carlo model. The Pine Forest Range is well-constrained by field observations, and most model parameters are described by relatively narrow ranges of geologically reasonable values. The model suggests an average slip rate of ~1.1 km/Myr and an onset of faulting ca. 9-10 Ma, compared to rates of 0.3-0.8 km/Myr and initiation ca. 11-12 Ma derived from visual inspection of the data. The geometry of the East Range fault block is less well-constrained by field observations, but the data nonetheless robustly support an approximately 6-fold reduction in extension rate at ~14 Ma, after faulting began at ~17 Ma with an extension rate of ~3 km/Myr. The absence of a preserved partial retention zone in the East Range sample set limits how well the model can predict fault dip and footwall geometry. This model is conducive to Bayesian parameter estimation to quantify the geological uncertainty in the geometry of the tilted fault block, and its simplicity and flexibility allow application to a wide variety of normal faults where cooling ages already exist or could potentially be collected.

Plain Language Summary

Normal faults form in settings where the crust is extending and can be associated with both seismic hazards and natural resource emplacement. To learn about the history of normal faults

we often turn to minerals that record the history of cooling that occurs as fault slip carries rocks from depth to the relatively cool surface of the Earth. To interpret these cooling histories, it is common practice to treat the cooling of these minerals as resulting from the vertical translation of a series of samples through the crust. However, this ignores the basic geologic observation that sets of samples are often collected from areas that have undergone rotation as well as vertical translation. Here we investigate how this rotation may complicate the interpretations we make about fault histories by simulating the cooling histories of minerals that undergo faulting and associated rotation. We find that traditional methods for inferring slip histories on faults may be significantly biased and propose a relatively simple alternative for investigating these systems that is consistent with our geologic observations.

1 Introduction

Low-temperature thermochronometry—primarily apatite fission-track (AFT) dating and apatite (U-Th)/He (AHe) dating—is an effective and widely-used tool for establishing the timing and rate of slip on normal faults, because it directly records cooling of the rising footwall block during fault slip (Stockli, 2005). Rates of exhumation, fault slip and extension are often derived from suites of footwall thermochronometer samples by regressing plots of age vs. elevation (Armstrong et al., 2003), age vs. distance from the fault trace (Foster & John, 1999; Miller et al., 1999), or age vs. inferred sample depth prior to unroofing ("structural depth") relative to some geologic datum (Colgan et al., 2004; Fitzgerald et al., 1991; Howard & Foster, 1996; Stockli, 2005; Stockli et al., 2000).

Many active and ancient normal faults are the boundaries between tilted fault blocks, in which the adjacent footwall and hanging wall blocks tilt—along with the fault plane—as slip accrues on the fault (Proffet, 1977). Examples abound in the geologic record, often referred to as "domino-style" normal faults. Thermochronometer ages from such fault systems are often interpreted in the context of inferred structural depth, with fault slip and exhumation rates derived from the slope of the age vs. structural depth trend and the initiation of faulting inferred from the "inflection point" on the edge of inferred AHe partial retention zone (PRZ) or AFT partial annealing zone (PAZ) (see review in Stockli, 2005). The inferred position of the PAZ/PRZ is also frequently used to estimate the geothermal gradient at the onset of faulting

(Colgan, Dumitru, McWilliams, et al., 2006; Fitzgerald et al., 1991; Foster et al., 1991; Howard & Foster, 1996; Stockli et al., 2002; Surpless et al., 2002).

However, simple regression of age vs. structural depth (or distance from the fault plane) fails to account for the fact that rocks collected at the surface today from a progressively tilted fault block experienced curved particle trajectories and variable magnitudes of velocity during fault slip. The effects of heat advection and erosion within the fault block are not taken into account (see Ehlers et al., 2001), and "eyeballing" the position of the PAZ/PRZ can be inaccurate and often depends on the age and estimated position of just one or two samples. Here, we assess how the curved trajectories followed by samples from a tilted normal fault block affect the interpretations derived from low-temperature thermochronometers.

We present a simple formulation of the thermal evolution of a rotating fault block driven by a constant extension rate. Constant extension requires that slip rates decline as fault dips shallow and a greater component of slip is parallel to the extension direction (conversely, assuming a constant fault slip rate over time would imply a changing extension rate). The advection of heat and perturbation of geothermal gradients by topography influence thermal fields and the thermal histories of exhumed particles (e.g., Ehlers et al., 2003), but we find that for a range of conditions typical of active normal faults these effects yield AHe ages that are comparable to those derived from rotation through a fixed temperature field.

As a result of a reduction in slip rate and the curved particle paths predicted by rotation, age - structural depth plots only provide satisfactory estimates for the average geologic slip rate (the total displacement divided by the duration of faulting) for certain fault geometries. The age of the oldest sample below the PRZ/PAZ (often a proxy for the initiation of faulting) can over- or underestimate the initiation time by several million years. In light of these findings, we use the simplified solution of rotation through a fixed temperature field to assess two natural examples, demonstrating the utility of our model for deriving quantitative estimates of deformation rates and other parameters (timing of faulting, geothermal gradient) from suites of thermochronometer ages from tilted fault blocks.

2 Cooling of a rotating fault block

2.1 Impacts of rotation alone

We derive the evolution of temperatures and the exhumation of rock by assuming the velocity field of the upper crust is governed by the rotation of a series of rigid blocks with inclined boundaries that slide smoothly past one another (Fig. 1). For each fault block we assume that rotation occurs about a fixed axis on the topographic surface at the midpoint of the block (Fig. 1). Geologically, this point corresponds to the transition from eroded footwall bedrock to basin fill or preserved pre-faulting strata at the edge of the adjacent basin. In this model, the amount of rotation, θ, on a fault block is dependent on the integrated extension rate, *e* [Lt^-1],

1. $$\theta = \alpha - \sin^{-1}\left(\frac{-W_0 sin\alpha}{\int_0^t e\, dt + W_0}\right).$$

Where α is the initial dip of the fault, *e* is the extension rate [Lt^{-1}] on a single fault, *t* is the time since the start of faulting, and W_0 [L] is the width of a fault block. For simplicity, we assume a constant extension rate such that the amount of rotation is given as

2. $$\theta = \alpha - \sin^{-1}\left(\frac{-W_0 sin\alpha}{et + W_0}\right).$$

and the total displacement along a fault, *S*, is given by:

3. $$s = (et\ +\ W_0)\sqrt{(1 - (\frac{-W_0 sin\alpha}{et+W_0})^2} - W_0 cos\alpha$$

An important consequence of our assumption of a constant extension rate is that the fault-parallel slip rate decreases as the fault shallows. Both the geologically measured, time-averaged slip rate (*S/t*) and the instantaneous slip rate, *dS/dt,*

4. $$\frac{dS}{dt} = \frac{eW_0^2 \sin^2\alpha}{(et + W_0)^2\sqrt{(1 - \frac{W_0^2 \sin^2\alpha}{(et+W_0)^2}}} + e\sqrt{1 - \frac{W_0^2 \sin^2\alpha}{(et+W_0)^2}},$$

decrease through time, therefore the instantaneous slip rate will always be less than the average slip rate (Fig. 2 A). The deviation between the time-averaged slip rate and the instantaneous slip rate depends on the parameters describing the system (Fig. 2 B). All the examples in Figure 2 display a maximum discrepancy between average and instantaneous slip rates of ~20% (for an initial fault of 65°), but the rate at which that misfit is reached depends on the magnitude and duration of rotation.

To illustrate how thermochronometer ages record rotation and the decrease in slip rate required to maintain a constant extension rate on rotating faults, we first construct cooling histories from rotation through a static temperature field. Given time invariant, surface parallel isotherms that describe a constant geothermal gradient, dT/dy [TL^{-1}], the history of temperatures, $T(t)$, of a mineral rotated with the fault block can be described as the rotation through that geothermal gradient:

$$5.\quad T(t) = -(X sin\theta + Y cos\theta)\frac{dT}{dy} + T_s.$$

Here X, Y describe the initial coordinates of minerals relative to the axis of rotation of the fault block (Fig. 1). Here we take the rotation axis of fault blocks to be at the surface, where the temperature is T_s, and in the middle of the fault block. From here on we will refer to the thermal histories and resultant thermochronometer ages predicted by Eqn. 5 as the 'fixed-isotherm model'.

We examine thermal histories for evenly spaced points collected at the surface between the rotation axis and the fault contact bounding the uplifted footwall (Fig. 3 A). We focus on the apatite U-Th/He (AHe) system, and predict the impact of these cooling histories on thermochronometer evolution by implementing the solution for a spherical thermochronometer described by (Ketcham, 2005). For simplicity we restrict these simulations to 50 µm radius, spherical apatites with the diffusion kinetics of Farley (2000), and with initial ^{238}U,^{235}U, ^{232}Th concentrations of 22.0,22.0/137.0,49.0 ppm. These concentrations and grain sizes represent averages of measurements obtained from three sample suites collected from Mesozoic and Cenozoic granitic rocks in the Basin and Range (Colgan et al., 2010; Colgan, Dumitru, Reiners, et al., 2006; Fosdick & Colgan, 2008). Age-structural depth plots and radial concentration profiles from these models are shown in Figure 3 C & D.

We explore how the rotation of particle paths impacts the interpretation of AHe ages in a series of synthetic experiments. We simulate the ages and structural depths of 50 "samples," whose final positions are evenly spaced between the hinge of the fault block and the bounding fault (the uplifted domain in our configuration). We define a base case of a 20 km wide fault block, extending at a rate of 1 km / Myr, and rotating 25°, and independently vary the block width, extension rate, and rotation magnitude about this case (Fig. 4). We prepend an isothermal holding duration (here out t_{hold}) of 10 Ma to the thermal history of each sample. We calculate an exhumation rate from age-depth regressions of data that began below the PRZ (e.g., those samples from depths where temperatures are at least 90° C) and define the predicted start of faulting as the age of the oldest sample included in this regression. We compare these rates to the actual average slip rate (e.g. S/t) and the actual duration of faulting with the difference between predicted and expected values normalized by expected values (Fig. 4). The exhumation rate derived from age-depth regressions is not expected to reflect the slip rate in most settings, as it is a measure of unroofing given a steady thermal field and not a direct record of fault motion (Ehlers et al., 2001). Past efforts have attempted to transform the exhumation rate measured from thermochronology to a fault slip rate (e.g. based on fault dip, see Stockli, 2005 and references therein). Here we choose to compare slip rates directly to exhumation rates because exhumation rates remain the most readily derived proxy for fault motion in most normal fault studies.

2.1.1 Results: Influence of rotation on thermochronometer inferences

In the case of horizontal, invariant isotherms the rotation of the fault block (Fig. 3 A) results in curvilinear T-t paths that converge in temperature as they rotate toward the surface (Fig. 3 B). The angle between particle trajectories and isotherms will initially be relatively oblique and rotate to be orthogonal as particles approach the surface (Fig. 3 A). Given constant rotation rates this would result in increasing cooling rates toward the surface, as particles come to take a shorter path between isotherms. However, in our experiments we see the opposite behavior due to our description of rotation as a function of a constant extension rate (Fig. 3 B). As fault dip becomes shallower, a greater component of extension is resolved for an equivalent magnitude of slip, requiring a reduction in slip rate assuming the extension rate stays constant (Fig. 2 A), and in turn a reduction in the velocity of particles toward the surface. As a consequence of being farther from the rotation axis (Fig. 1), particles exhumed from greater structural depth in our model have faster average cooling rates (Fig. 3 B).

Modelled AHe ages have stepped age-structural depth relationships similar to observations from natural systems (Stockli, 2005, Fig. 3 C). The example in Fig. 3 C shows the best fit between age and structural depth for those samples that resided at temperatures > 90° C and a gray shaded region depicting the expected exhumation relationship for samples starting within the partial retention zone (defined here broadly between 40° and 80° C, Stockli et al., 2000) and exhuming at the average slip rate (S/t). In this example, the inferred exhumation rate corresponds well to the average slip rate however the initiation of faulting pre-dates the oldest simulated AHe age below the partial retention zone (Fig. 3 C).

We highlight discrepancies between inferred (from interpretation of AHe ages) and model parameters for a range of configurations in Fig. 4. If the start of faulting is interpreted to be the youngest AHe age below the partial retention zone, as it is here, then the initiation of faulting will often be significantly underestimated (e.g., 10% - 30 % difference, Fig. 4), although this may change for configurations not examined here (e.g., given the trend in Fig. 4 A). For a 10 km wide fault block with a geothermal gradient of 25° C/ km, exhumation rates provide a good estimate of geologic slip rates given low extension rates and narrow fault blocks (Fig. 4), bearing in mind that these will be greater than the present, instantaneous rate of slip (Fig. 2). For wider fault blocks and for extension rates >0.5 km/Myr exhumation rates underpredict expected geologic slip rates (Fig. 4 A & B). For a 10 km fault block rotating through a fixed temperature field, exhumation was not great enough for us to infer exhumation rates or the initiation of faulting with less than ~25° of rotation (Fig. 4 C).

2.2 Impacts of heat advection and topographic growth

While the example discussed above is a useful illustration of the relationship between block rotation, fault slip rate, and AHe ages, it neglects important components of the thermal evolution of the rotating fault block. Here we assess how the growth of long-wavelength topography and the advection of heat by crustal movement influence thermochronometer ages from tilted fault blocks. We describe the thermal evolution of faulted crust as the competition between conductive cooling, governed by a thermal diffusivity D [L^2t^{-1}], and the advection of heat with the movement of rock, governed by the product of the velocity field $\boldsymbol{V}$ [Lt^{-1}] and the local temperature gradient, ∇T. Unlike past work (e.g. Ehlers et al., 2001; Ehlers & Chapman, 1999) we ignore the local production of heat and the potential for heat transport by fluids in order to focus on the impact of advection and topographic growth, which are absent from the simple solution for rotation through fixed isotherms,

6. $\frac{dT}{dt} = D\nabla^2 T + \boldsymbol{V} \cdot \nabla T.$

We integrate the above equation in two dimensions, the fault perpendicular (extension parallel) direction and depth, effectively assuming symmetry in the along strike direction. We calculate the first and second-derivatives of temperature with first-order, downwind and second-order finite difference approximations, respectively, and integrate the model with a simple forward-euler scheme with a fixed time step. To ensure stability we set the time step to be less than the minima of the stable time steps determined for advection and diffusion. From here on we will refer to the thermal histories and resultant AHe ages predicted by Eqn. 6 as the 'thermo-kinematic model'.

2.2.1 Boundary conditions

We simulate a region 50% wider than the final rotated width of the fault block, W_f (Fig. 1 C) and restrict our analysis of thermal histories to the central block. At the left and right boundaries we create additional temperature columns to calculate derivatives, and assign these temperature columns the temperature values from the equivalent position in the central block (Fig. 1 B). While there is the expectation for some differences between the thermal histories of the different fault blocks we simulate (because the non-central blocks are being advected laterally away from the central block), we feel that this effect is likely to be minor when focusing on thermal histories observed in the central block. At the base of the model we prescribe a fixed flux, Q_{base}, which we assign based on the diffusivity and prescribed initial geothermal gradient.

The evolution of the topographic surface presents a more complicated boundary condition. At and above the topographic surface we apply a fixed temperature, T_{surf} (10° C). Past work has highlighted how surface topography deflects subsurface temperature gradients and can influence thermochronometer cooling histories (Ehlers et al., 2001; Reiners, 2007; Reiners & Brandon, 2006). It is the longest-wavelengths of topography that produce the deepest temperature perturbations and are therefore most likely to be recorded by thermochronometers. For this reason we ignore more detailed descriptions of topographic evolution that attempt to describe particular geomorphic forms (e.g. the stream-power equation to describe bedrock river incision, Whipple et al., 2000) in favor of a simple approach that produces long-wavelength topography.

Erosion rates scale with local relief, and therefore average slope (Ahnert, 1970), suggesting that landscapes will evolve toward an equilibrium to balance erosion rates and rock uplift. Therefore, in rotating normal fault blocks we might expect that relief will evolve as slip rates evolve and that the wavelength of high topography will broaden as the fault block relaxes and its intersection with Earth's surface broadens. To achieve these effects in our models we assert that erosion rate scales linearly with slope according to a constant, k [Lt^-1], and that the local topography is in steady state such that erosion rates are equal to the vertical component of the velocity field:

$$7. \quad \frac{dz}{dx} = \frac{V_y}{k}.$$

Here we calculate V_y along the fault block at the elevation of the rotation axis. We integrate $\frac{dz}{dx}$ up from the hanging-wall footwall contact and from the rotation axis, and assign local elevations as the minimum of these integrations in different directions (Fig. 5). We assume all regions with downward (e.g. subsiding) vertical velocities are immediately covered by sediment up to the elevation of the rotation axis. We do not let topography exceed the bounding elevations of the fault plane or a planar, rotating datum representing the flat initial topography. This approach ignores the horizontal component of surface velocities, does not conserve mass, and neglects important details of landscape evolution that control the rate and form of topographic evolution. However, it produces model fault-block geometries similar to natural examples and serves as a starting point to assess if and how low-temperature thermochronometers are sensitive to the evolution of topography in a tilted footwall block. In addition, the use of Eqn. 7 limits the complexity of the model and produces topography with a relatively realistic appearance.

2.2.2 *Exploring realistic scenarios*

Based on examples drawn from the Basin and Range province of western North America we explore two base cases for normal fault kinematics. First we examine the case of rapid slip (>3 km/Myr.) on closely-spaced faults (3-5 km apart) that tilt from initial angles of 60-70º to dips <20º (Colgan et al., 2010; Fitzgerald et al., 2009; Reiners et al., 2000; Surpless et al., 2002; Wong & Gans, 2003). Second are slower slip (<1 km/Myr) systems on more widely spaced faults (20-30 km) that rotate from initial dips of 60-70º to 40-50º (Armstrong et al., 2003; Colgan, et al., 2006; Fosdick & Colgan, 2008; Lee et al., 2009; Stockli et al., 2003). These base cases are not intended to be comprehensive, but to represent the range of tilt magnitudes and slip rates typical of continental extensional fault systems where thermochronology has been applied.

We explore the impact of developing topography and advective heat transport on AHe ages to assess if and when the simplification of rotation through fixed isotherms (Eqn. 5) provides a satisfactory description of low-temperature thermochronometer ages. We do so by independently varying individual parameters of interest for two base cases: 1) closely-spaced faults that undergo large rotations during rapid strain (Fig. 6, Table. 1), and 2) widely-spaced faults that undergo moderate rotation during much slower strain (Fig. 7, Table. 2). We vary those parameters which are expected to move thermal histories away from the expectations of the rotation through flat isotherms solution (Fig. 3). We vary the erosion coefficient, *k,* to produce relief and consequently deflect subsurface isotherms, we decrease the thermal diffusivity, *D,* to increase the importance of advective heat transport, and we vary the extension rate, *e*, to simultaneously increase topographic relief and the contribution of advection to heat transport. In modelling low-temperature thermochronometer ages we assign an arbitrary 15 Ma of pre-faulting isothermal holding to calculated time-temperature paths to produce the curves characteristic of age vs. structural depth plots (e.g. Fig. 3 C).

2.2.2 *Results: Impact of rotation, advection, and topographic growth on thermochronometer ages*

We present comparisons between the fixed-isotherm solution and thermo-kinematic model (e.g. Eqn. 5) for the narrow and wide fault base cases in Figures 6 & 7. In these comparisons, samples experience the same particle trajectories, but are assigned a constant surface temperature once they are advected above the fixed-isotherm model (Fig. 3). Absolute age differences are larger in the wider, more slowly extending fault blocks (Fig. 7 A, D, &G) than the narrow, rapidly extending case (Fig. 6 A, D, & G), but the relative difference in modelled AHe ages are comparable. In the narrow fault case the resulting topography produces a minimal deflection of the isotherm corresponding to the effective closure temperature of apatite (Fig. 6, bottom row), although topographic development and an increase in the relative contribution of advection to temperature changes causes a noticeable shallowing of the effective closure isotherm. For wider fault blocks, the thermo-kinematic model predicts that the greater width and height of the resultant topography yields larger subsurface temperature perturbations beneath the uplifting portion of the fault block (Fig. 7, bottom row). For most samples the difference in the modelled AHe ages between the simple rotation case and the thermo-kinematic model is on the order of the typical reproducibility of AHe ages from a given sample (e.g. <10%, Reiners et al., 2005; Vermeesch, 2010) for all the parameters varied. However, in the case of narrow, rapidly extending fault blocks we observe discrepancies between AHe ages calculated from the thermo-kinematic model and the fixed-isotherm model that exceed 10% for the most deeply exhumed samples (Fig. 6, middle row). The most significant relative differences are seen in cases where advection of heat is important relative to diffusion, and where exhumation has exposed deep samples that have more cooling in this perturbed thermal field. This is most evident in the more rapidly moving 'narrow' fault block case (Fig. 6), where both increases in extension rate and decreases in *D* cause large deviations from the fixed-isotherm thermal field and large differences (up to ~18%) between predicted AHe ages. In cases of narrow and wide fault blocks the misfit between the fixed-isotherm model and the thermo-kinematic model tends to increase with structural depth, with progressively younger ages derived from the thermo-kinematic model as a function of depth.

The deviation between the modelled AHe ages in the fixed isotherm and thermo-kinematic models reflects the evolving nature of the thermal field away from the initial condition of a constant geotherm. Samples exhumed from the greatest depth experienced the most cooling in a temperature field that deviates from that predicted by the fixed-isotherm model. In addition, the deepest samples are also farthest from the rotation axis and therefore have the highest velocities, increasing the importance of advection relative to diffusion on the thermal field. This is perhaps best reflected in the Fig. 6 E, where low diffusivities combined with rapid extension rates produce the greatest discrepancy between real and modelled ages (~18%). However, for the expected diffusivity of many of the granitic rocks studied with AHe thermochronnology,~10^{-6} m^2/s or ~30 m^2/yr (Whittington et al., 2009), and for <~5 Km of exhumed structural depth, the differences between the solutions computed for representative apatite grains remains comparable to or less than the level of (2 σ) precision currently typical of U-Th/He dating (Reiners et al., 2005), notwithstanding the common problem of over dispersion in AHe datasets. This is particularly true for slower rates of extension (e.g. < 3 km/Myr) and less rotated fault blocks (e.g. < 45°), as seen in Figure. 7, where only in the most extreme cases do the predictions of the thermo-kinematic and fixed isotherm models differ by > 10%. Additionally, both solutions, and in particular the wide fault block example, show that for a range of conditions simple regressions of age vs. structural depth would not accurately predict the initiation or rate of fault slip (Fig. 4, 6 A,D,G, & 7 A,D,G).

3 Application to real data

Motivated by the observed discrepancies between age-structural depth regressions and rates of fault slip (Fig. 4), we utilize the predictions of the simple rotation model to solve for the parameters that best characterize datasets from natural systems. There are undoubtedly cases where advection (Ehlers et al., 2001, 2003; Willett & Brandon, 2002), topographic growth and decay (Reiners, 2007; Valla et al., 2011), and other processes unaccounted for in this model (such as fluid flow, Ehlers & Chapman, 1999) are reflected in thermochronometers ages. However, the simplicity of this solution allows us to assess the correspondence between observations of cooling recorded in thermochronometers and our conceptual model of normal fault kinematics efficiently and with a relatively small number of free parameters. Specifically, we seek to fit observed AHe ages with predictions from the simple rotation model in order to determine those model parameters that best reproduce our observations. Unlike past work that employed a similar approach (Ehlers et al., 2003), our model takes into account the evolving fault geometry and horizontal motions expected from rigid block rotation.

In describing AHe ages, the fixed isotherm model is constrained by two sets of observations; field observations (e.g. observed fault dips, stratigraphic dips, and positions of samples) and AHe ages. We describe the sample locations in terms of their structural depth (relative to a pre-faulting geologic horizontal datum) and location relative to the current surface trace of the bounding fault (Fig. 8). We compare observed and modelled structural depths and AHe ages to describe both the geometric characteristics of the fault block (e.g. its width and the magnitude of rotation) and the cooling history of the samples. Specifically, we utilize a Monte Carlo approach. For each Monte Carlo step we guess a suite of parameters (θ, α, W_b, e, $\frac{dT}{dy}$, t_{hold}), based on these parameters and the observed, modern locations of samples we back-rotate samples to their initial location in the crust. From the back-rotated sample coordinates we then forward integrate the history of rotation, cooling, and He production and diffusion predicted by these parameters. While we can theoretically measure some of these parameters directly with field observations (e.g. the fault dip and the amount of rotation), we choose to leave them as free parameters as quality checks on the model. As with the comparisons between the fixed-isotherm model and thermo-kinematic model (Fig. 6 & 7), samples that are advected above the elevation of the bounding fault are assigned the surface temperature (here 10° C). The thermo-kinematic model highlights that while this is an oversimplification, these positions within the crust are associated with temperatures well below the effective closure temperature of AHe (Farley, 2000), resulting in a relatively minor bias to computed AHe ages for a range of conditions (Fig. 6 & 7).

To evaluate uncertainties on model parameters we employ a Bayesian, Markov chain Monte Carlo (MCMC) approach, using an affine- invariant ensemble sampler (Foreman-Mackey et al., 2013; VanderPlas, 2014). In this approach for each modelled parameter set we must calculate the product of a *prior* and a *likelihood*. The *prior*, *P(F)*, captures our confidence in the values of model parameters before collecting data, here F refers to our model with a given set of parameters (θ, α, W_b, e, $\frac{dT}{dy}$, t_{hold}). The *likelihood*, *P(D|F)*, describes the probability of obtaining our observed AHe ages and structural depths (our data, *D*) given our model with a set of parameters. We use the *prior* and *likelihood* to determine the probability of model parameters given our data and model (the *posterior* probability, *P(F|D)*) through random sampling. It is worth emphasizing the meaning of the values and uncertainties obtained from this method; we do not account for the uncertainty we have in the model we present for rotation driven exhumation - the probability distributions we obtain reflect the uncertainty in model parameters *given* that model. In other words, what is the probability of an extension rate given that extension rate remained constant and drove rotation of rigid fault blocks which in turn produced an observed pattern of AHe ages?

Unless otherwise noted, we utilize a uniform *prior*,

8. $\ln\big(P(F)\big) = 0,$

effectively asserting that prior to collecting our data we had equal confidence in any particular parameter value. Philosophically this is an oversimplification; for example, before ever sampling a normal fault block we would have some idea of what the geothermal gradient might be based on other studies in the region and global observations. We also have some information about the initial dip of the fault and the amount of rotation based on geologic information (Fig. 8), and we will explore introducing these insights in a second example. However, some of this information is also present in estimates of the structural depth of samples and their positions in the cross-section. In using a uniform *prior* we seek to explore those model solutions that describe the data with minimal influence from our initial expectations.

We characterize the *likelihood* of our observations as the product of independent gaussian distributions for the calculated age and measured structural depth,

$$9. \quad \ln\big(P(D|F)\big) = \sum_{j=0}^{k} \ln\left(\frac{1}{\sqrt{2\pi\sigma_{A,j}^2}} e^{-\frac{\left(A_{obs,j}-A_{mod,j}\right)^2}{2\sigma_{A,j}^2}}\right) + \ln\left(\frac{1}{\sqrt{2\pi\sigma_{Z,j}^2}} e^{-\frac{\left(Z_{obs,j}-Z_{mod,j}\right)^2}{2\sigma_{Z,j}^2}}\right)$$

Here k is the number of AHe ages modelled (24 ages from 12 samples, Fig. 8), A_j denotes one of the observed and modelled AHe ages (denoted by $_{obs}$ and $_{mod}$ respectively), $\sigma_{A,j}$ is the analytical uncertainty on that grain age. The observed and modelled structural depths are Z_j and the observations are given a relative uncertainty of 5%, $\sigma_{Z,j}$. The relative uncertainty in structural depths represents our decreasing confidence in depths as we move down section, away from observed stratigraphic markers. To model AHe ages for each sample we utilize the average of the radii and parent isotope concentrations computed from the suite of samples.

3.1 Application to the Pine Forest Range, NV

We apply this approach to a transect of published AHe ages from the Pine Forest Range, a typical Neogene Basin and Range fault block in northwestern Nevada, USA (Colgan, Dumitru, McWilliams, et al., 2006; Colgan, Dumitru, Reiners, et al., 2006; Fig. 8) whose cooling history was also explored by Gallagher (Gallagher, 2012). The Pine Forest Range is a west-tilted block of Cretaceous (115-108 Ma) granitic rocks unconformably overlain by Tertiary (ca. 16-30 Ma) volcanic and minor sedimentary rocks (Colgan, Dumitru, McWilliams, et al., 2006). Samples for AHe and AFT analysis were collected along an east-west transect perpendicular to the east-dipping normal fault that bounds the east side of the Pine Forest Range fault block and have a mean radius of 66 μm and parent concentrations of 21 ppm ^{238}U and 36 ppm ^{232}Th. . Field observations of the exposed fault plane constrain its present dip to ~40º (Colgan, Dumitru, Reiners, et al., 2006), and geologic mapping and dating of the Tertiary volcanic section indicate the range was tilted ~30º W after ca. 16 Ma (Colgan, Dumitru, McWilliams, et al., 2006). Colgan, Dumitru, Reiners, et al., (2006) interpreted AFT and AHe ages from these samples to record Late Cretaceous exhumation and cooling followed by Cenozoic tectonic quiescence prior to mid-Tertiary volcanism, with slip on the range bounding fault beginning ca. 11-12 Ma and continuing to the present at a loosely-inferred fault slip rate of 0.3–0.8 Ma. A pre-extensional geothermal gradient of 27 ± 5ºC/km was estimated from a plot of age vs. estimated structural depth of these samples.

3.2 Results from the Pine Forest Range, NV

We run the MCMC model for a total of 240,000 iterations, distributed over 40 'walkers' (each walker takes 6,000 guided steps through the parameter space), and trim a burn-in period of 1,000 iterations from each walker in characterizing the *posterior* distribution. We initialize the model with parameter guesses drawn from a Gaussian distribution with a standard deviation of 5% about mean initial guesses (α= 70°, θ= 30°, W_b = 14 km, e = 0.7 km/Myr, $\frac{dT}{dy}$= 27° C/ km, t_{hold} = 40 Myrs, Fig. 9). The means of these initial guesses were selected based on field observations (Colgan, Dumitru, McWilliams, et al., 2006) and a minimization routine between observed and expected AHe ages for those parameters not directly measureable from cross sections. Results are presented in Figure 9 and 10. In the first few hundred iterations the sample chain diverges from the initial guesses noticeably for nearly all the parameters except the initial dip of the fault (*alpha*, Fig. 9). While some of these parameters re-converge around our initial estimates, the isothermal holding duration and geothermal gradient vary about new values. In the case of all parameters, the sample chain appears stable after the burn in period. A different set of initial mean guesses (α= 60°, θ= 30°, W_b = 10 km, e = 1 km/Myr, $\frac{dT}{dy}$= 25° C/ km, t_{hold} = 40 Myrs) with a wider random initial variation (10%) converged around the same parameter estimates. However, with these wider, random initial guesses a subset of parameter combinations produced solutions that did a poor job of replicating the patterns observed in the data, resulting in incalculably low *likelihoods* and the MCMC sampler getting 'stuck' on these bad conditions.

The most-likely parameter configuration identified for the Pine Forest Range (Fig. 10) was not directly evaluated in the comparisons of the fixed-isotherm and thermo-kinematic models presented in Fig. 6 & 7, although the parameters determined for the Pine Forest Range are similar to those presented in Fig. 7 (Table. 2). Conducting the model comparison experiments for the median set of parameters observed after the burn-in period revealed a <10% error of AHe ages predicted by the thermo-kinematic and fixed isotherm models for all samples below the PRZ, within the PRZ the two models predicted as much as ~11% differences in AHe. The pattern of relative error as a function of structural depth observed for the modelled Pine Forest parameter set is similar to the observed in the base case of Figure 7 (B, E, H).

Age-structural depth relationships observed and those derived from the model are shown in Figure 11 A. Models do a good job of reproducing the observed pattern in ages. Unlike a linear regression fit to samples below a rollover at ~2.5 km depth, the model appears less sensitive to a pair of samples at ~3.2 km depth that are slightly older than the closest points upsection. We plot some inversion results comparable to the local geology in Figure 8. Insets A, B, and C on the cross section (Fig. 8) highlight the modelled position of the hinge (located half of the final, surface fault block width from the fault trace), the total rotation (the expected dip of stratified units deposited prior to faulting), and the current dip of the fault. From our proposed model (Fig. 1) and prior intuition we would have expected the best fitting rotation axis to be located at the boundary between tilted, pre-faulting units and basin fill but the best fitting rotation axis (specified by $W_f/2$) is slightly offset from this point (Fig. 8). However, the overall geometry of the fault block is well described by the modelled parameters. This is a reflection of the fact that we jointly infer parameters to describe both AHe ages and structural depths, the latter of which are determined from cross sections.

Strong covariances between many of the parameters are highlighted in Fig. 10. For steeper initial fault dips, slower extension rates and wider fault blocks are required to explain the observations, but isothermal holding durations are relatively invariant. Similarly, wider fault blocks require less rotation. However, it is noteworthy that many of the parameters are constrained to a relatively narrow range in the realm of geologic possibilities.

We characterize the most likely initiation of faulting, *t*, and its uncertainty using the parameter sets sampled in the MCMC chain (e.g., Kruschke, 2013) with the following expression:

$$10.\ t = -\frac{W_b}{e}\left(\frac{\sin\alpha}{\sin(\theta - alpha)} + 1\right).$$

Figure 11 B highlights this result. Similarly, we can compute the distributions of the average slip rate through dividing the total slip *S* (Eqn. 3) by *t* (Eqn. 10) for each of the parameter sets in the MCMC chain. This average slip rate is significantly higher than the slope of the regression line. In the best-case scenario of normal fault slip causing the vertical advection of rock through fixed isotherms we would expect the exhumation rate revealed by the slope of age-structural depth data to be half the slip rate, however two times the age-depth regression is still only ~75% of the inferred slip rate (Fig. 11).

From an initial guess of about 40 Myr, the isothermal holding duration is fairly well constrained to ~70-80 Myr in the model (Fig. 9 & 10), despite the top of the partial retention zone not being recorded in AHe data (Fig. 11). Added to the modeled ~10 Myr history of faulting, this result suggests isothermal holding of the host pluton since about 80-90 Ma, remarkably similar to the cooling history derived independently from modeled AFT data, which Colgan, Dumitru, McWilliams, et al. (2006) interpreted to record exhumation of the pluton between 85-90 and 75 Ma, followed by isothermal holding prior to the onset of faulting. This result suggests that the shape of the age-depth curve through the PRZ may preserve recoverable information about the long-term pre-faulting thermal history of a fault block.

3.3 Application to the East Range, NV

The East Range is an east-tilted block of Paleozoic and Mesozoic sedimentary and igneous rocks, locally intruded by Cenozoic plutons and overlain unconformably by Cenozoic sedimentary and volcanic rocks (Fig. 12 D). Samples for AFT and AHe analysis (Fig. 13 A) were collected from an Oligocene (31 Ma, U-Pb) granitic pluton that intrudes the pre-Tertiary basement, along an E-W transect perpendicular to the west-dipping normal fault that bounds the west side of the East Range block (Fosdick and Colgan, 2008). This fault is not exposed and there are no direct constraints on its dip. At the latitude of the AFT and AHe samples, tilted Cenozoic strata are not exposed in direct contact with basement, but Oligocene to early Miocene sedimentary rocks and tuffs dip 30-45º east in the nearby Sou Hills, which Fosdick and Colgan (2008) interpreted as an approximation of the total East Range block tilt. About 5 km north of their sample transect, basement rocks are overlain by basalt flows as young as 13-14 Ma (Nosker, 1981) that dip ~15º east. Fosdick and Colgan (2008) interpreted field relationships and AFT and AHe ages from this sample transect to record rapid slip on the range-bounding fault ca. 17–15 Ma, which resulted in tilting of the Oligocene and early Miocene sedimentary and volcanic rocks, with poorly constrained slip on the same fault after 10 Ma that resulted in tilting of the 13 Ma basalt flows. A pre-extensional geothermal gradient of ~23ºC/km was estimated from a plot of age vs. estimated structural depth of these samples, in which only the fission-track PAZ was preserved. Beyond noting that the middle Miocene event was “rapid” and the younger one less so, Fosdick and Colgan (2008) did not attempt to determine actual slip or extension rates, and noted that it was "unclear, at present.. if there was a significant time gap… between rapid Middle Miocene extension and the onset of late Miocene high-angle faulting."

To describe the two-phase faulting history inferred for the East Range we employ the same MCMC approach as in the Pine Forest Range, NV but consider an expanded set of parameters (α, W_b, $\frac{dT}{dy}$, t_{hold}, t_1, t_2,, e_1, e_2). In this model, faulting begins at time t_1 with an extension rate of e_1, and proceeds until a time of t_2 when an extension rate of e_2 begins. We use the more general form of Eqn. 1 to derive the amount of rotation at each time in the model history rather than the constant extension rate required by Eqn. 2.

We present the results of MCMC modelling with two sets of priors. First, we use a series of relatively uninformative priors, we refer to this as the 'minimally constrained' model. In the minimally constrained model there is 0 probability of extension rates, fault block widths, and isothermal holding durations that are not positive and finite. Similarly, in this first configuration, there is 0 probability of fault dips outside of the range 0-90° and initiations of faulting, t_1, that occur after the change in extension rate, t_2. We believe that geothermal gradients outside of the range 0 – 70 ° C/km are unreasonable, and we assign these a 0 probability. Finally, the age of the pluton that hosts these samples is 31.4 ± 0.4 Ma (1σ), and therefore we describe the probability of the total history of the samples ($t_{hold} + t_1$) as 1 less the cumulative density function of the Gaussian distribution described by the pluton age and uncertainty.

For the second set of priors, which we refer to as the 'informative priors' model we preserve the same constraints on all other parameters, but introduce a Gaussian prior for the geothermal gradient and the initial fault dip. A survey of past efforts that estimated pre-extensional geothermal gradients from the Basin and Range suggests a mean gradient of 22.0° C/km and a standard error of 1.6° C/km (Colgan et al., 2008, 2010; Colgan, Dumitru, McWilliams, et al., 2006; Colgan, Dumitru, Reiners, et al., 2006; Fitzgerald et al., 2009; Fosdick & Colgan, 2008; Foster & John, 1999; Howard & Foster, 1996; Lee et al., 2009; Reiners et al., 2000; Stockli et al., 2002, 2003; Surpless et al., 2002). Andersonian mechanics predicts initial dips of normal faults similar to those commonly observed in natural settings, so we assert that the probability of fault dips is described by a Gaussian distribution about this value (60° ± 3°). If the AHe data provides tight constraints on the fault block geometry (as observed with the Pine

Forest Range, Fig. 8 & 10) the posterior probability will be updated from the prior. While observed normal fault dips certainly deviate from the narrow range we assign, we choose to introduce this as a prior in part to demonstrate the co-dependence of different parameters and how geologic knowledge of the fault block geometry can be used to constrain the inferred faulting history.

Conceptually, one could imagine also introducing a non-uniform *prior* for the total amount of rotation of the fault block (θ) based on field observations of tilted stratigraphy. However, structural depths are often inferred (as done here) from projections of stratigraphic datum and therefore introducing an additional constrain on θ would effectively be introducing the same information again.

3.3 Results from the East Range, NV

We run both the minimally constrained and informative prior models for 8,000 iterations after an initial burn-in of 2,000 iterations with 40 walkers (resulting in a total of 320,000 samples from the post burn-in period that characterize the *posterior* probability, Fig. 14). From our initial guesses (α= 60°, W_b = 20 km, $\frac{dT}{dy}$= 23° C/ km, t_{hold} = 4 Myrs, t_1 = 17 Myr, t_2 = 13 Myr, e_1 = 3 km/Myr, e_2 = 0.3 km/Myr), the sample chain diverges and begins to explore initially lower values of α, W_b, t_1, t_2, and e_1 with complementary changes in other parameters (Fig. 14). However, in the informative priors case this exploration is quickly limited as the sample chain encounters the lower probabilities of small fault dips (and of large geothermal gradients) introduced by our priors on these values. In both examples, the isothermal holding duration (t_{hold} ≈ 0 – 15Ma, note that the total time predicted for AHe samples is $t_{hold} + t_1$) is unconstrained within the bounds allowed by the age of the pluton that hosts the samples (Fosdick & Colgan, 2008). Both models make narrow predictions for the total amount of rotation despite variability in other aspects of the fault block geometry (Fig. 12), because the assigned structural depths are derived from this quantity.

In the minimally constrained model, the *posterior* distributions define broad probabilities for the fault block width, geothermal gradient, and initial fault dip. However, these broad ranges described by the *posterior* are narrower than the total range we allowed for, suggesting that even in this example the AHe data and sample positions provide some minimal information about fault block geometry. For example, fault dips below ~30° are not observed in the *posterior* (despite being allowed to vary from 0-90°, Fig. 12 & 14). Similarly, despite being allowed to vary from 10° - 70°, geothermal gradients below ~20° C are not observed in the *posterior*; too low of a geothermal gradient would place the upper samples within or above the partial retention zone, which is not observed (Fig. 14).

In the informative priors example, the posterior distribution on the initial fault dip and geothermal gradient is not updated from our prior characterization of these quantities (Fig. 14), highlighting that the AHe ages from the East Range provide little insight into these parameters. The restriction of the fault dip (α) and geothermal gradient ($\frac{dT}{dy}$) have the added consequence of limiting the allowable fault block width (W_b), as both the fault dip and fault block width control the rotation history of the fault block (Fig. 1). The expected final half-width of the rotated block (and thus the position of the rotation axis relative to the bounding fault's contact with the surface), is ~18.5 km (Fig. 12 C). This lies somewhere between the point where the asserted Oligocene land surface and the projected base of Miocene basalts intersect the surface (Fig. 12 D). It is important to note that given the model for rotation presented here (Fig. 1) these two datums should intersect the surface at the same point. Perhaps the predicted values of $W_f/2$ that lie between the Miocene basalts and Oligocene land surface reflects an average rotation axis for the samples. Alternatively, the rotation model (Fig. 1) might not accurately describe the true kinematics of the uplift and rotation of the East Range. The most likely ~22 km fault block would occupy a current cross-sectional width of ~37 km given its rotation (Fig. 12 C). This distance extends from the current fault contact across the Tobin Range to the east. Either this prediction is spurious, or the modern Tobin Range is a geologically younger fault block whose bedrock was part of the East Range tilt block in the middle Miocene—a surprising, but testable geologic hypothesis revealed by the model. In addition, transformation of the *posterior* distributions suggest ~17- 30 km of slip, significantly more than previous estimates from reconstructed cross sections (Fosdick & Colgan, 2008).

Despite containing minimal information about the geometry of the fault block, the East Range AHe data provide good constraints on the initiation and rates of extension (Fig. 13 B). In both the minimally constrained and informative priors models, the *posterior* probability of the initiation of faulting (t_1) is restricted to ~18 Ma & ~17 Ma, respectively (Fig. 13 & 14), and a reduction in extension rate from ~3 km/Myr to 0.6 km/Myr at ~14 Ma is most likely (Fig. 13 &

14). However, while the informative priors do narrow the *posterior* distribution of the parameters describing the history of extension in the East Range, both model setups predict a second (albeit less likely) configuration of parameters that are also able to reproduce the observed data. We highlight these two configurations in Fig. 14 (orange and green arrows) and plot their predictions in Fig. 13. Both configurations must reproduce the assigned structural depths for each sample and adequately predict AHe ages, but this is accomplished with different tectonic histories. In the more likely configuration, an initially relatively rapid extension rate is short in duration and followed by a more moderate extension rate (Fig. 13 B, orange line). The East Range data can also be explained by relatively moderate initial extension rates that span almost the entire history of faulting (Fig. 13 B, green line), although from the *posterior* distributions this configuration is less likely.

4 Discussion/ Conclusion

We computed predicted AHe ages from time-temperature paths calculated from a kinematic description of rigid fault block rotation (Eqn. 5) with a constant geothermal gradient. Modeled age patterns highlight that in rotated fault blocks it is not straightforward to derive rates of fault slip and extension from exhumation rates estimated from linear regressions of age vs. inferred structural depth. Models also indicate that the oldest sample from definitively below the partial retention zone commonly underestimates the initiation of faulting (Fig. 4). The discrepancy between the modelled start of rotational faulting and that inferred from age-structural depth plots in both our fixed-isotherm and thermo-kinematic models highlights that even in fault systems where exhumation histories are apparently well resolved (e.g., Colgan, Dumitru, McWilliams, et al., 2006; Colgan, Dumitru, Reiners, et al., 2006), quantitative descriptions of fault block kinematics can revise our understanding of the chronology of geologic events.

The model of rotation through fixed isotherms ignores the effects of topographic growth and advection on thermal evolution, processes of demonstrable importance in the cooling of rocks and the evolution of thermochronometer ages (Ehlers et al., 2001). The discrepancies between modelled age-structural depth data and the expectation if age-depth regressions revealed the onset and rate of slip (ball-ended line segments, Figs. 6 & 7, A, D, G) are greater for the thermo-kinematic models (dashed lines, Figs. 6 & 7, A, D, G) than the fixed isotherm models (solid line, Figs. 6 & 7, A, D, G). This suggests that when topographic growth and advection influence thermal histories, estimates of the initiation of normal faulting may be more biased than our fixed isotherm simulations suggest (Fig. 4). This discrepancy grows larger for samples exhumed from greater depths, which undergo more cooling in a perturbed thermal field. However, we show that differences in AHe ages between the full thermo-kinematic model and the fixed-isotherm model (Fig. 6 & 7) are within the range of typical AHe precision for a range of geologically reasonable topographic reliefs, extension rates, and efficiencies of diffusive heat transfer.

Our modeling offers some insight into where samples can be collected to maximize the amount of information about deformation rates in rotated normal fault blocks. Sampling transects that traverse significant structural relief proximal to the range front may limit the impact of variable exhumation paths (Fig. 3A), but sampling will always be subject to real-world constraints of time, resources, access, and the availability of apatite-bearing rocks. Samples from the pre-faulting PRZ not only preserve information about the pre-faulting cooling history and geothermal gradient but can also constrain the geometry of the fault block to a surprising degree (Fig. 10). Every effort should be made to sample this part of the fault block when investigating the initiation of faulting, up to the pre-faulting topographic surface if it is preserved. The effects of topography and diffusive heat transfer are often small in the examples studied here, but they tend to be more pronounced for samples exhumed from greater depths (Fig 6 & 7). The most deeply exhumed samples also record the most cooling resulting from young faulting, hence studies that wish to examine samples from these settings in detail should take care to consider the possible effects of perturbed geothermal gradients.

The spatial context of samples can be incorporated into general methods for inverting thermochronology data for thermal histories (Gallagher, 2005), which provides a more flexible approach for treating data than imposing a particular deformation history. In the case of the Pine Forest Range, this results in a more complicated thermal history than our constant extension rate, fixed isotherm model can predict (Gallagher, 2012). In addition these more flexible approaches often incorporate more sophisticated models of He diffusion in apatite that consider the impacts of accumulating radiation damage on He retentivity (Flowers et al., 2009; Shuster et al., 2006). These rules would be important for interrogating the pre-faulting history potentially recorded by samples at low structural depths, but we expect them to have minimal impact on the parts of the sample transect that record relatively rapid cooling (e.g., ~10° C/Myr or more, Fig. 3 B) from below the partial retention zone (Flowers et al., 2009) which we are most interested in here.

In the Pine Forest Range, parameters revealed by Markov chain Monte Carlo inference are described by relatively narrow ranges of parameters in the realm of geologic possibility (Fig. 8), although there are often strong covariances between parameters (e.g. the extension rate and initial fault dip). Our model of the Pine Forest Range suggests an average slip rate of ~1.1 km/Myr; significantly higher than the exhumation rate derived from the slope of the age-structural depth regression (0.41 km/Myrs) (Fig. 11 A & C). In the case of the Pine Forest Range the expected initiation of faulting derived from the model (~9-10 Ma), is slightly younger than the 11-12 Ma suggested by previous work (Colgan, Dumitru, Reiners, et al., 2006).

In an example from the East Range, Nevada, we add complexity to the kinematic model by allowing the extension rate to change once during the history of fault slip. The resulting model suggests faulting initiated at ~17 Ma in the East Range, with a decrease in extension rate from ~3 to ~0.5 km/Myrs at ~14 Ma. This change in rate reproduces an observed 'kink' in the age-structural depth relationship of these samples, although another, less likely solution describes the tectonic history with a lower initial extension rate that extends until ~6 Ma (Fig. 13). Despite the PRZ not being preserved in that data set, the model provides a relatively precise prediction for the start of faulting that is similar to independent estimates derived from joint modelling of AHe and AFT data (Fosdick & Colgan, 2008).

Many of the geometric parameters in the East Range model (Fig. 14) are poorly constrained and/or can accommodate solutions within most of the range we define as allowable. In contrast, results from the Pine Forest Range are tightly constrained, due to the PRZ being preserved in the data set, the ages being tightly grouped, and the apparently simple tectonic history. Introducing additional constraints to the East Range model in the form of prior assessments of the initial fault dip and geothermal gradient refines the *posterior* probability of some of these parameters (Fig. 12 & 14), but does not significantly alter the histories of extension predicted by the model (Fig. 13). In addition, the East Range model predicts a Miocene fault block width greater than the observed modern width. Using the rotation model to understand the geologic history of this range must therefore confront the question of whether the model of rigid rotation about the center of single fault block (Fig. 1) is appropriate for this setting.

Inverse modeling can recover useful information about tectonic histories and their uncertainty when the cooling histories of sample suites are linked by a kinematic model. Although our model of fault block rotation ignores rheological properties of rocks and the evolving stress state of the crust (Olive et al., 2016; Thompson & Parsons, 2016), it produces evolving velocity fields consistent with expectations from reconstructed cross sections and is true to the common conceptual model of exhumed thermochronometers in normal faults (Miller et al., 1999; Stockli, 2005). While these models could be used to make inferences about geologic structure (e.g., fault dip in Fig. 8 & 12), they are no substitute for primary observations of the local geology collected from geologic mapping and measurements of the stratigraphy and structure of the fault block in question. First, the solutions we present are dependent on estimates of structural depth. Second, the kinematic model we present is itself derived from primary geologic observations of normal faults (e.g., Proffet, 1977). Third, as the East Range example demonstrates (Fig. 13 & 14), improved characterization of the observable geology of the system (e.g., through understanding of the fault dip), in turn improves predictions of tectonic history. Thus, above all, our modeling highlights the well-known importance of geologic context for interpretation of samples.

Acknowledgments, Samples, and Data

AHe data for the Pine Forest Range samples can be found in Figure 8 or in Colgan, Dumitru, Reiners, et al., (2006). AHe data from the East Range can be found in Figure 6 of Fosdick and Colgan (2008). This manuscript benefitted from detailed and insightful reviews by Richard Lease, Ryan McKeon, Jason Ricketts, and associate editor Sean Long. This work was supported by the USGS National Cooperative Geologic Mapping and Mineral Resources Programs. This draft manuscript is distributed solely for purposes of scientific peer review. Its content is deliberative and predecisional, so it must not be disclosed or released by reviewers. Because the manuscript has not yet been approved for publication by the U.S. Geological Survey (USGS), it does not represent any official USGS finding or policy. Any use of trade, firm, or product names is for descriptive purposes only and does not imply endorsement by the U.S. Government.

References

Ahnert, F. (1970). Functional relationships between denudation, relief and uplift in large mid-latitude drainage basins. *American Journal of Science*, *268*, 243–263.

Armstrong, P. A., Ehlers, T. A., Chapman, D. S., Farley, K. A., & Kamp, P. J. J. (2003). Exhumation of the central Wasatch Mountains, Utah: 1. Patterns and timing of exhumation deduced from low-temperature thermochronology data. *Journal of Geophysical Research: Solid Earth*, *108*(B3). https://doi.org/10.1029/2001JB001708

Colgan, J. P., Dumitru, T. A., & Miller, E. L. (2004). Diachroneity of Basin and Range extension and Yellowstone hotspot volcanism in northwestern Nevada. *Geology*, *32*(2), 121–124. https://doi.org/10.1130/G20037.1

Colgan, J. P., Dumitru, T. A., Reiners, P. W., Wooden, J. L., & Miller, E. L. (2006). Cenozoic Tectonic Evolution of the Basin and Range Province in Northwestern Nevada. *American Journal of Science*, *306*(8), 616–654. https://doi.org/10.2475/08.2006.02

Colgan, J. P., Dumitru, T. A., McWilliams, M., & Miller, E. L. (2006). Timing of Cenozoic volcanism and Basin and Range extension in northwestern Nevada: New constraints from the northern Pine Forest Range. *Bulletin of the Geological Society of America*, *118*(1–2), 126–139. https://doi.org/10.1130/B25681.1

Colgan, J. P., John, D. A., Henry, C. D., & Fleck, R. J. (2008). Large-magnitude Miocene extension of the Eocene Caetano caldera, Shoshone and Toiyabe Ranges, Nevada. *Geosphere*, *4*(1), 107–130. https://doi.org/10.1130/GES00115.1

Colgan, J. P., Howard, K. A., Fleck, R. J., & Wooden, J. L. (2010). Rapid middle Miocene extension and unroofing of the southern Ruby Mountains, Nevada. *Tectonics*, *29*(6). https://doi.org/10.1029/2009TC002655

Ehlers, T. A., & Chapman, D. S. (1999). Normal fault thermal regimes: conductive and hydrothermal heat transfer surrounding the Wasatch fault, Utah. *Tectonophysics*, *312*(2–4), 217–234. https://doi.org/10.1016/S0040-1951(99)00203-6

Ehlers, T. A., Armstrong, P. A., & Chapman, D. S. (2001). Normal fault thermal regimes and the interpretation of low-temperature thermochronometers. *Physics of the Earth and Planetary Interiors*, *126*(3–4), 179–194. https://doi.org/10.1016/S0031-9201(01)00254-0

Ehlers, T. A., Willett, S. D., Armstrong, P. A., & Chapman, D. S. (2003). Exhumation of the central Wasatch Mountains, Utah: 2. Thermokinematic model of exhumation, erosion, and thermochronometer interpretation. *Journal of Geophysical Research: Solid Earth*, *108*(B3). https://doi.org/10.1029/2001JB001723

Farley, K. a. (2000). Helium diffusion from apatite: General behavior as illustrated by Durango fluorapatite. *Journal of Geophysical Research*, *105*(B2), 2903–2914. https://doi.org/10.1029/1999JB900348

Fitzgerald, P. G., Fryxell, J. E., & Wernicke, B. P. (1991). Miocene crustal extension and uplift in southeastern Nevada: Constraints from fission track analysis. *Geology*, *19*(10), 1013. https://doi.org/10.1130/0091-7613(1991)019<1013:MCEAUI>2.3.CO;2

Fitzgerald, P. G., Duebendorfer, E. M., Faulds, J. E., & O'Sullivan, P. (2009). South Virgin-

White Hills detachment fault system of SE Nevada and NW Arizona: Applying apatite fission track thermochronology to constrain the tectonic evolution of a major continental detachment fault. *Tectonics*, *28*(2). https://doi.org/10.1029/2007TC002194

Flowers, R. M., Ketcham, R. a., Shuster, D. L., & Farley, K. a. (2009). Apatite (U-Th)/He thermochronometry using a radiation damage accumulation and annealing model. *Geochimica et Cosmochimica Acta*, *73*(8), 2347–2365. https://doi.org/10.1016/j.gca.2009.01.015

Foreman-Mackey, D., Hogg, D. W., Lang, D., & Goodman, J. (2013). emcee : The MCMC Hammer. *Publications of the Astronomical Society of the Pacific*, *125*(925), 306–312. https://doi.org/10.1086/670067

Fosdick, J. C., & Colgan, J. P. (2008). Miocene extension in the East Range, Nevada: A two-stage history of normal faulting in the northern basin and range. *Bulletin of the Geological Society of America*, *120*(9–10), 1198–1213. https://doi.org/10.1130/B26201.1

Foster, D. A., & John, B. E. (1999). Quantifying tectonic exhumation in an extensional orogen with thermochronology: examples from the southern Basin and Range Province. *Geological Society, London, Special Publications*, *154*(1), 343–364. https://doi.org/10.1144/GSL.SP.1999.154.01.16

Foster, D. A., Miller, D. S., & Miller, C. F. (1991). Tertiary history in the Old Woman Mountains Area, California: Evidnce from apatite fission track data. *Tectonics*, *10*(5), 875–886.

Gallagher, K. (2005). Exploiting 3D Spatial Sampling in Inverse Modeling of Thermochronological Data. *Reviews in Mineralogy and Geochemistry*, *58*(1), 375–387. https://doi.org/10.2138/rmg.2005.58.14

Gallagher, K. (2012). Transdimensional inverse thermal history modeling for quantitative thermochronology. *Journal of Geophysical Research: Solid Earth*, *117*(2), 1–16. https://doi.org/10.1029/2011JB008825

Howard, K. A., & Foster, D. A. (1996). Thermal and unroofing history of a thick, tilted Basin-andRange crustal section in the Tortilla Mountains, Arizona, *101*, 511–522.

Ketcham, R. a. (2005). Forward and Inverse Modeling of Low-Temperature Thermochronometry Data. *Reviews in Mineralogy and Geochemistry*, *58*(1), 275–314. https://doi.org/10.2138/rmg.2005.58.11

Kruschke, J. K. (2013). Bayesian estimation supersedes the t test. *Journal of Experimental Psychology: General*, *142*(2), 573–603. https://doi.org/10.1037/a0029146

Lee, J., Stockli, D. F., Owen, L. A., Finkel, R. C., & Kislitsyn, R. (2009). Exhumation of the Inyo Mountains, California: Implications for the timing of extension along the western boundary of the Basin and Range Province and distribution of dextral fault slip rates across the eastern California shear zone. *Tectonics*, *28*(1). https://doi.org/10.1029/2008TC002295

Miller, E. L., Dumitru, T. A., Brown, R. W., & Gans, P. B. (1999). Rapid miocene slip on the Snake Range-Deep Creek Range fault system, east-central Nevada. *Bulletin of the Geological Society of America*, *111*(6), 886–905. https://doi.org/10.1130/0016-7606(1999)111<0886:RMSOTS>2.3.CO;2

Nosker, S. A. (1981). *Stratigraphy and structure of the Sou Hills, Pershing County, Nevada*. University of Nevada, Reno.

Olive, J. A., Behn, M. D., Mittelstaedt, E., Ito, G., & Klein, B. Z. (2016). The role of elasticity in simulating long-term tectonic extension. *Geophysical Journal International*, *205*(2), 728–743. https://doi.org/10.1093/gji/ggw044

Proffet, J. M. (1977). Cenezoic geology of the Yerington distric, Nevada, and implications for the nature and origin of Basin and Range faulting. *Geological Society of America Bulletin*, *88*(70212), 247–266. https://doi.org/10.1130/0016-7606(1977)88<247

Reiners, P. W. (2007). Thermochronologic Approaches to Paleotopography. *Reviews in Mineralogy and Geochemistry*, *66*(1), 243–267. https://doi.org/10.2138/rmg.2007.66.10

Reiners, P. W., & Brandon, M. T. (2006). Using Thermochronology To Understand Orogenic Erosion. *Annual Review of Earth and Planetary Sciences*, *34*(1), 419–466. https://doi.org/10.1146/annurev.earth.34.031405.125202

Reiners, P. W., Brady, R., Farley, K. A., Fryxell, J. E., Wernicke, B., & Lux, D. (2000). Helium and argon thermochronometry of the Gold Butte block, south Virgin Mountains, Nevada. *Earth and Planetary Science Letters*, *178*(3–4), 315–326. https://doi.org/10.1016/S0012-821X(00)00080-7

Reiners, P. W., Ehlers, T. A., & Zeitler, P. K. (2005). Past, Present, and Future of Thermochronology. *Reviews in Mineralogy & Geochemistry*, *58*, 1–18. https://doi.org/10.1016/j.jmig.2010.03.005

Shuster, D. L., Flowers, R. M., & Farley, K. A. (2006). The influence of natural radiation damage on helium diffusion kinetics in apatite. *Earth and Planetary Science Letters*, *249*(3–4), 148–161. https://doi.org/10.1016/j.epsl.2006.07.028

Stockli, D. F. (2005). Application of Low-Temperature Thermochronometry to Extensional Tectonic Settings. *Reviews in Mineralogy and Geochemistry*, *58*, 411–448. https://doi.org/10.2138/rmg.2005.58.16

Stockli, D. F., Farley, K. a., & Dumitru, T. a. (2000). Calibration of the apatite (U-Th)/He thermochronometer on an exhumed fault block, White Mountains, California. *Geology*, *28*(11), 983. https://doi.org/10.1130/0091-7613(2000)28<983:COTAHT>2.0.CO;2

Stockli, D. F., Surpless, B. E., Dumitru, T. A., & Farley, K. A. (2002). Thermochronological constraints on the timing and magnitude of Miocene and Pliocene extension in the central Wassuk Range, western Nevada. *Tectonics*, *21*(4). https://doi.org/10.1029/2001TC001295

Stockli, D. F., Dumitru, T. A., Mcwilliams, M. O., & Farley, K. A. (2003). Cenozoic tectonic evolution of the White Mountains, California and Nevada. *GSA Bulletin*, *115*(4), 788–816. https://doi.org/10.1130/0016-7606(2003)115<0788:CTEOTW>2.0.CO;2

Surpless, B., Stockli, D. F., Dumitru, T. A., & Miller, E. L. (2002). Two-phase westward encroachment of Basin and range extension into the northern Sierra Nevada. *Tectonics*, *21*(1), 2-1-2–13. https://doi.org/10.1029/2000TC001257

Thompson, G. A., & Parsons, T. (2016). Vertical deformation associated with normal fault systems evolved over coseismic, postseismic, and multiseismic periods. *Journal of Geophysical Research: Solid Earth*, *121*(3), 2153–2173. https://doi.org/10.1002/2015JB012240

Valla, P. G., van der Beek, P. a., & Braun, J. (2011). Rethinking low-temperature thermochronology data sampling strategies for quantification of denudation and relief histories: A case study in the French western Alps. *Earth and Planetary Science Letters*, *307*(3–4), 309–322. https://doi.org/10.1016/j.epsl.2011.05.003

VanderPlas, J. (2014). Frequentism and Bayesianism: A Python-driven Primer. *ArXiv*, *astro-I*(Scipy), 1–9. Retrieved from http://arxiv.org/abs/1411.5018v1%5Cnfile:///Users/tomfinzell/Documents/Papers/2014/VanderPlas/arXiv 2014 VanderPlas.pdf%5Cnpapers://5fe7ecb3-5546-42c2-8572-990173724157/Paper/p3505

Vermeesch, P. (2010). HelioPlot, and the treatment of overdispersed (U-Th-Sm)/He data. *Chemical Geology*, *271*(3–4), 108–111. https://doi.org/10.1016/j.chemgeo.2010.01.002

Whipple, K. X., Hancock, G. S., & Anderson, R. S. (2000). River incision into bedrock: Mechanics and relative efficacy of plucking, abrasion, and cavitation. *Geological Society of America Bulletin*, *112*(3), 490–503. https://doi.org/10.1130/0016-7606(2000)112<490:RIIBMA>2.0.CO;2

Whittington, A. G., Hofmeister, A. M., & Nabelek, P. I. (2009). Temperature-dependent thermal diffusivity of the Earth's crust and implications for magmatism. *Nature*, *458*(7236), 319–321. https://doi.org/10.1038/nature07818

Willett, S. D., & Brandon, M. T. (2002). On steady states in mountain belts. https://doi.org/10.1130/0091-7613(2002)030<0175

Wong, M. S., & Gans, P. B. (2003). Tectonic implications of early Miocene extensional unroofing of the Sierra Mazata ´ n metamorphic core complex , Sonora , Mexico, (11), 953–956.

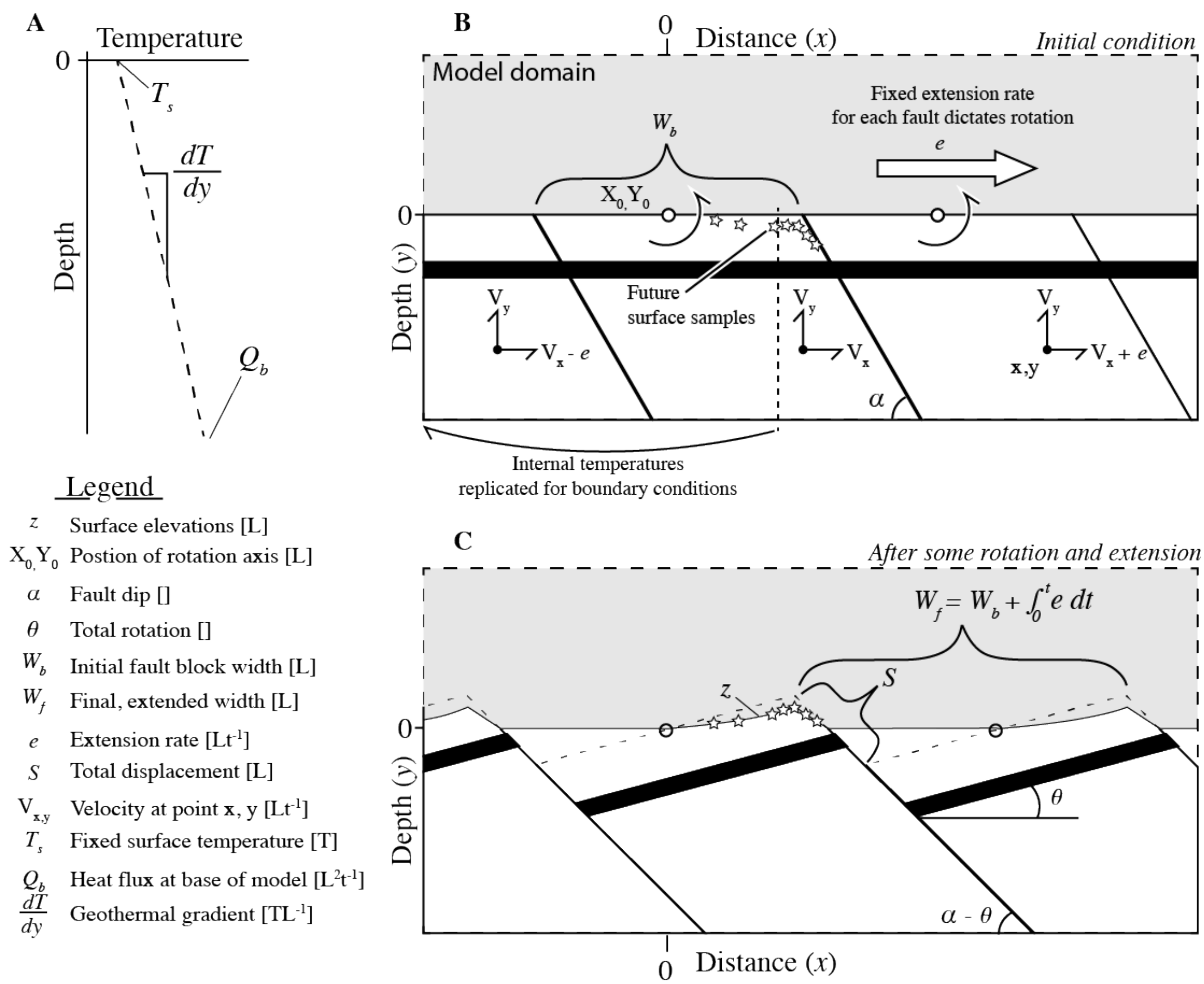

Figure 1. Illustration of the rotating fault block model and the terms used throughout the text. Panel **A** highlights a temperature profile into the crust. Panel **B** highlights the initial condition of a set of normal fault blocks before rotation, with a marker bed shown in black and areas above the land surface in grey. Panel **C** shows the same configuration after some extension has driven rotation and topographic growth.

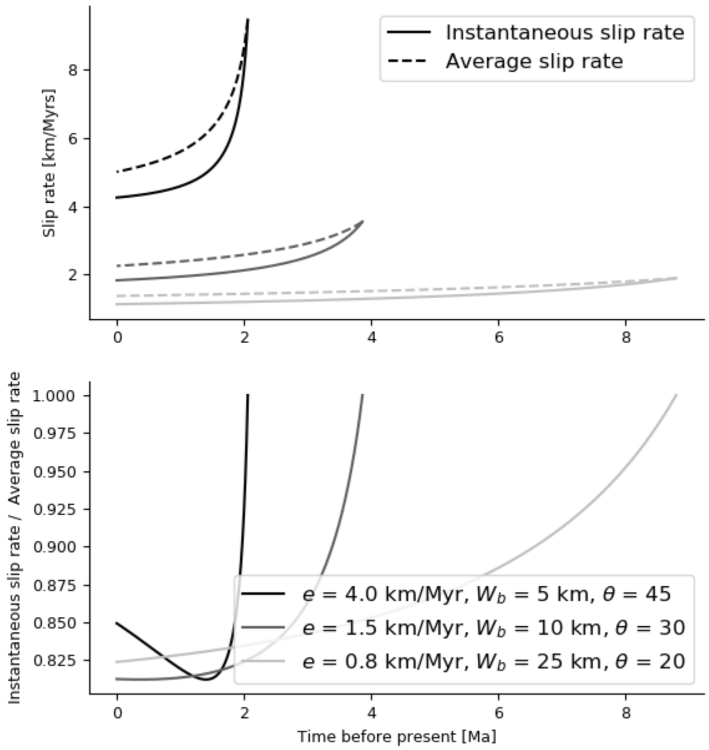

Figure 2. Comparison of instantaneous ($\frac{dS}{dt}$) and geologically averaged slip rates ($\frac{S}{t}$) for varying extension rates, fault block widths, and total amounts of rotation and an initial fault dip of 65°. Top panel depicts the actual values of each measure of slip rate, while the bottom panel depicts the ratio of the two.

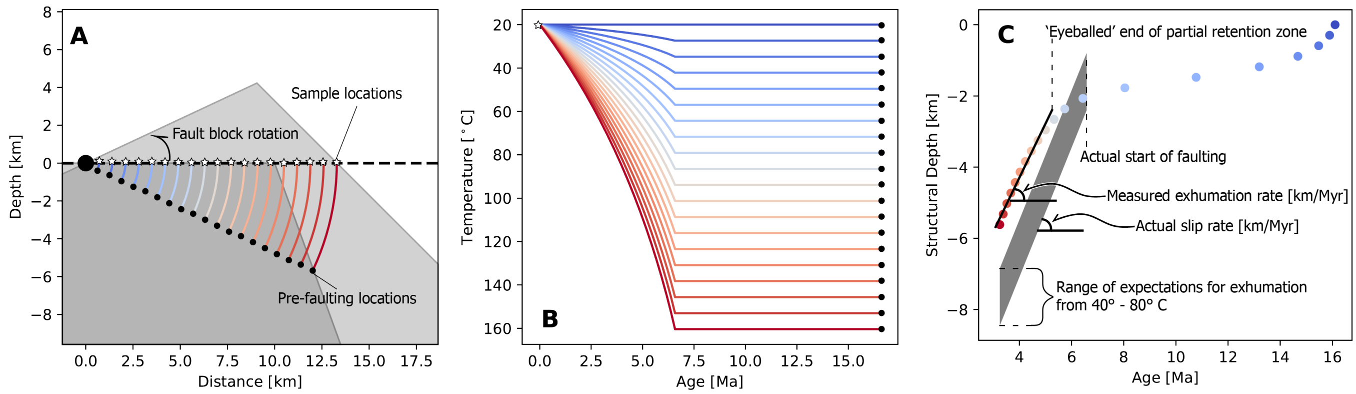

Figure 3. Example highlighting the rotation of particles in a rigid block driven by a constant extension rate. **A** depicts the rotation of particles in a rigid fault block (depicted as a grey polygon) bounded by faults with initial dips of 70° and experiencing an extension rate of 1 km/Myr along its bounding fault. Curved colored lines are particle paths, with colors representing individual particles depicted in other panels. Dashed line is the imposed flat topographic surface. Large, solid black circle is the imposed rotation axis, about which 25° of rotation occurs. Small black circles and stars are the initial, and final coordinates of a suit of simulated samples. **B** shows the time-temperature paths resulting from rotation through a 25°C/km geothermal gradient, plus an added 10 Ma of isothermal holding, and **C** shows the Apatite He ages that result from these cooling histories. In **C** the gray box shows the age-depth relationship for the average rate of fault slip, beginning at the initiation of faulting, for depths corresponding to temperatures of 40-80 ° C, while the solid black line in **C** is the best fitting age depth relationship for samples that are well outside of the partial retention zone (e.g. are associated with initial temperatures > 90° C).

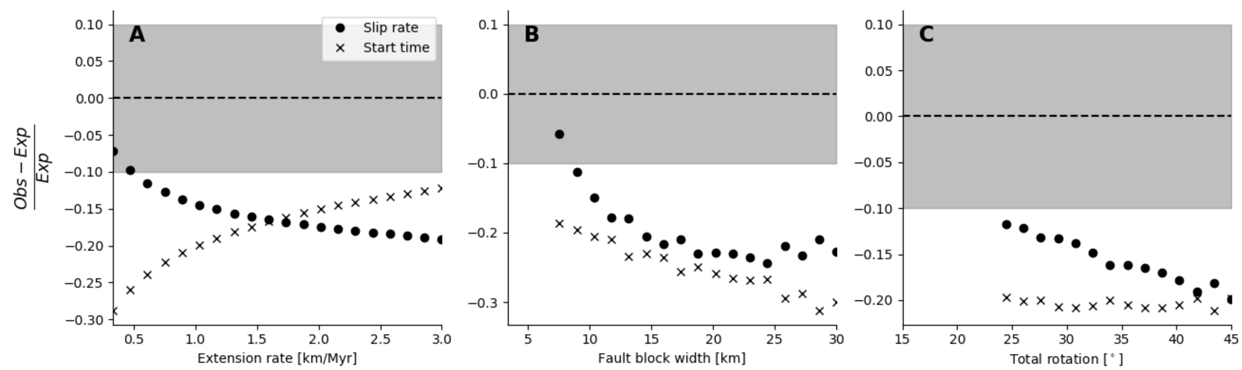

Figure 4. Comparison between model parameters and observations derived from interpretation of low-temperature thermochronology data. Gray bound denotes a +/- 10% relative error between observations and expectations. Observed slip rates are taken to be the exhumation rate estimates as the slope of age-depth regressions (computed for samples with initial temperatures > 90° C) and observed start times of faulting are taken to be the oldest age below the partial retention zone (e.g. the oldest sample with an initial temperature > 90° C, Fig. 3 C). Base configuration is a 10 km wide fault, extending at a rate of 1 Km/ Ma, to rotate a total of 30°, subplots **A**, **B**, and **C** show how variations in extension rate, fault block width, and the rotation magnitude about this base case impact observations. Changes to the total rotation and fault block width impact the initial location of samples prior to rotation (Fig. 3A), resulting in noise in the misfit functions in **B** and **C.**

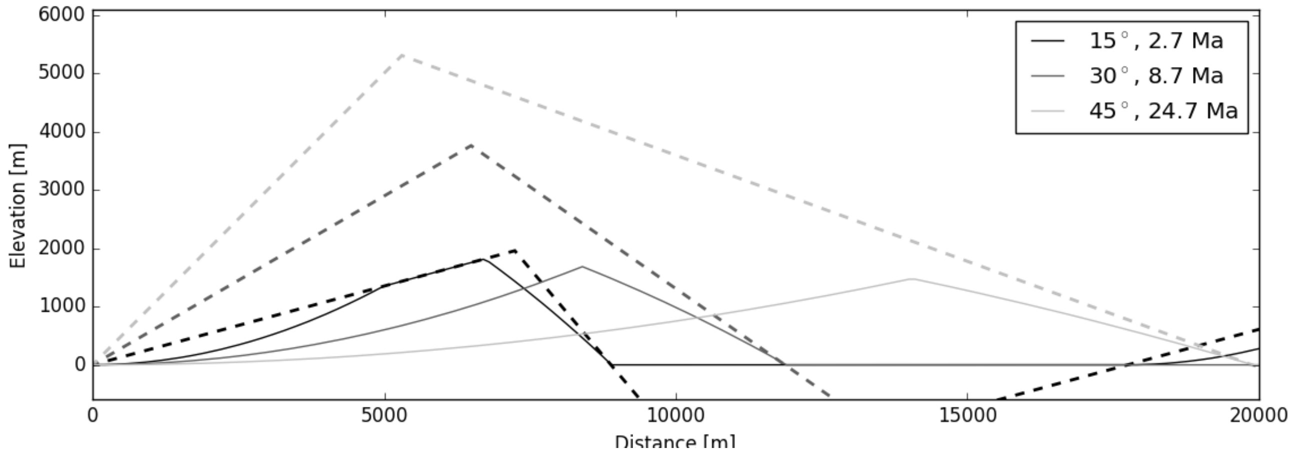

Figure 5. Example of the evolution of topography for k =12.5 mm yr^{-1}, an extension rate of 1 Km/ Myr, and a 15 Km wide fault block. Different colors show topography after different amounts of rotation have taken place, denoted in the legend by their amount of rotation and the time elapsed since the start of faulting. Dashed lines show the rotating boundaries of the fault block, solid lines show the topographic surface.

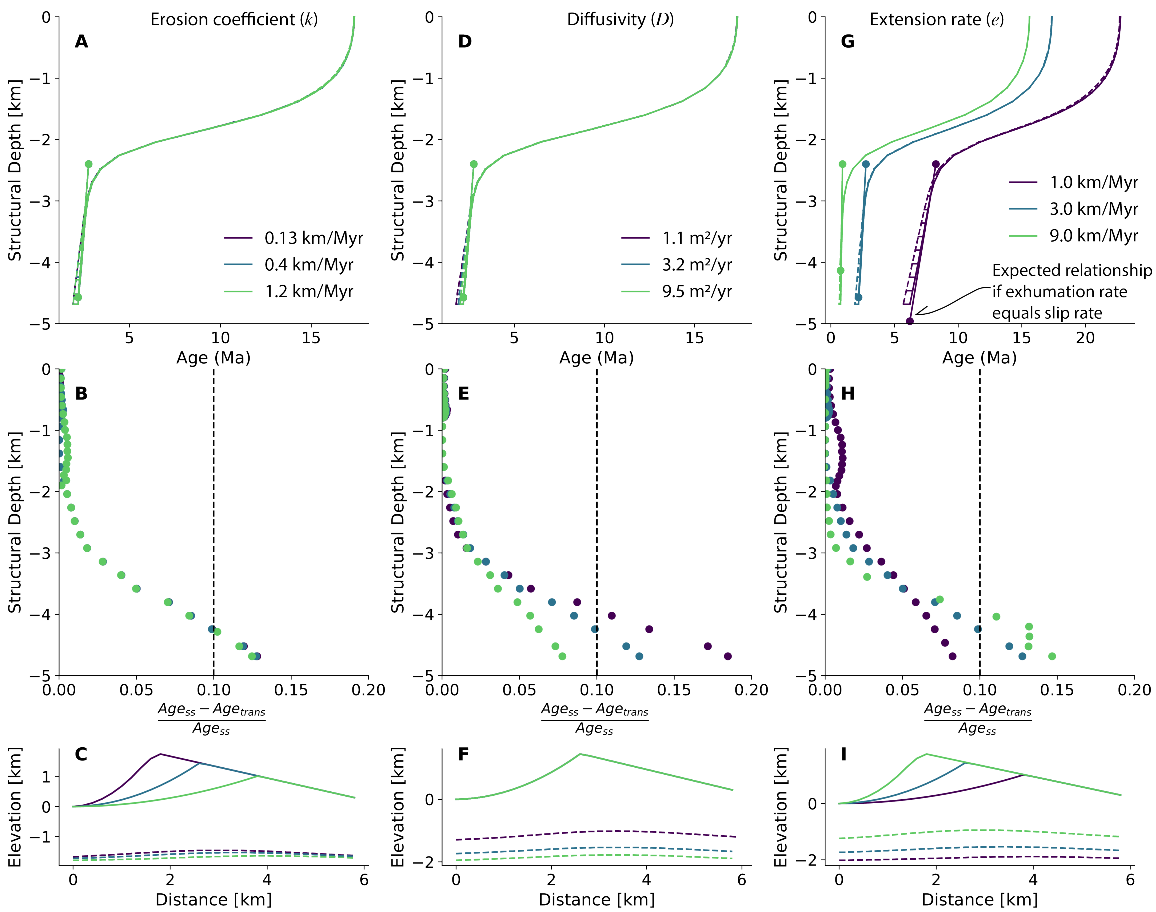

Figure 6. Comparison of modelled AHe ages for different model configurations given the 'narrow' fault block scenario. First, second, and third columns show results of varying a single parameter, the erosion coefficient [m/yr] (**A-C**), diffusivity [m^2/yr] (**D-F**), and extension rate [m/yr] (**G-I**), respectively. Top row shows plots of AHe age-structural depth for the thermo-kinematic model (dashed line) and the approximate solution for steady isotherms (solid line, e.g. Fig. 3). Middle row shows the relative error between the simulations; the difference between ages computed with the fixed isotherm model (*Age_{ss}*) and the thermo-kinematic model (*Age_{trans}*) normalized by ages of the fixed isotherm model. Positive values in the middle row indicate younger ages in the thermo-kinematic model. Bottom row highlights the profile of topography above a single fault block (solid line) and the corresponding 70° C isotherm (dashed line) at the end of the simulations. Base case parameters about which parameters were varied are described in Table 1.

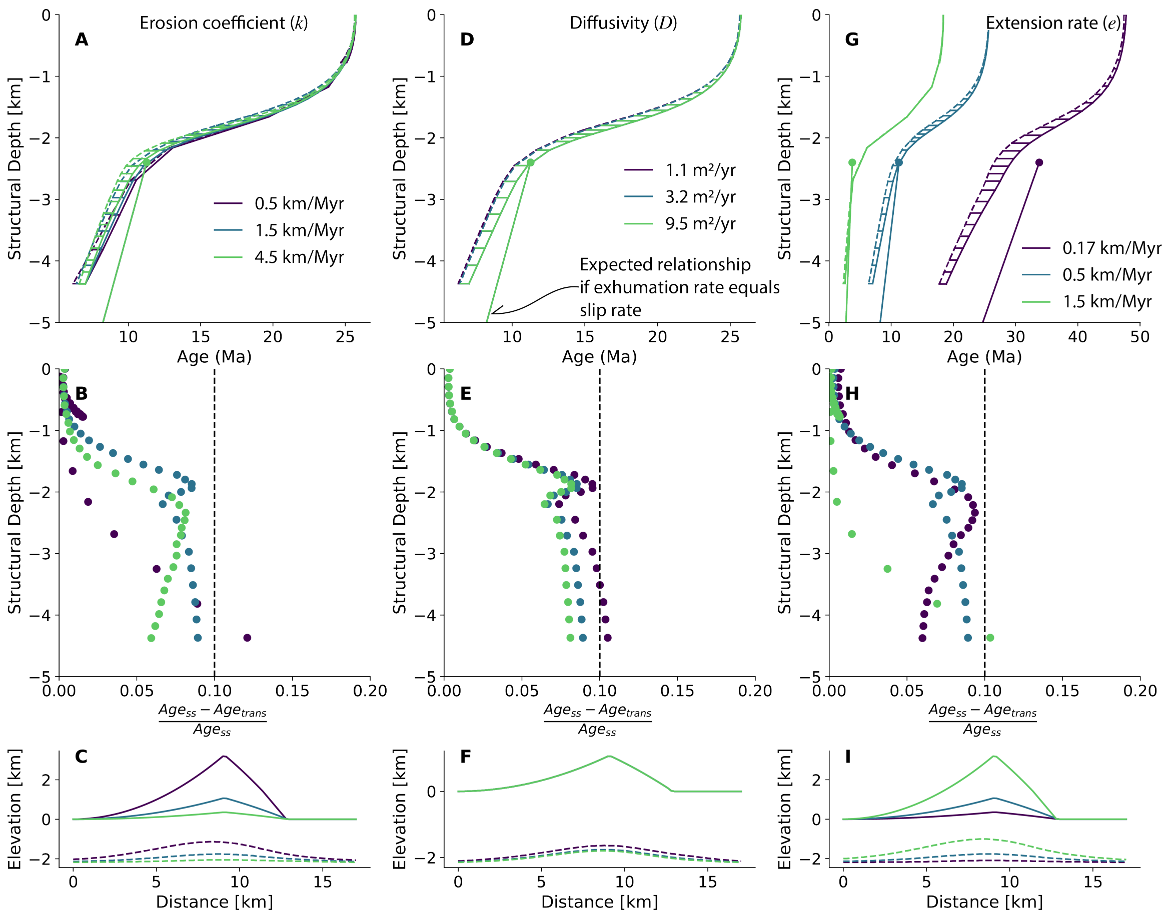

Figure 7. Comparison of modelled AHe ages for different model configurations given the 'wide' fault block scenario. First, second, and third columns show results of varying a single parameter, the erosion coefficient [m/yr] (**A-C**), diffusivity [m^2/yr] (**D-F**), and extension rate [m/yr] (**G-I**), respectively. Top row shows plots of AHe age-structural depth for the thermo-kinematic model (dashed line) and the approximate solution for steady isotherms (solid line, e.g. Fig. 3). Middle row shows the relative error between the simulations; the difference between ages computed with the fixed isotherm model (Age_{ss}) and the thermo-kinematic model (Age_{trans}) normalized by ages of the fixed isotherm model. Positive values in the middle row indicate younger ages in the thermo-kinematic model. Bottom row highlights the profile of topography above a single fault block (solid line) and the corresponding 70 °C isotherm (dashed line) at the end of the simulations. Base case parameters about which parameters were varied are described in Table 2.

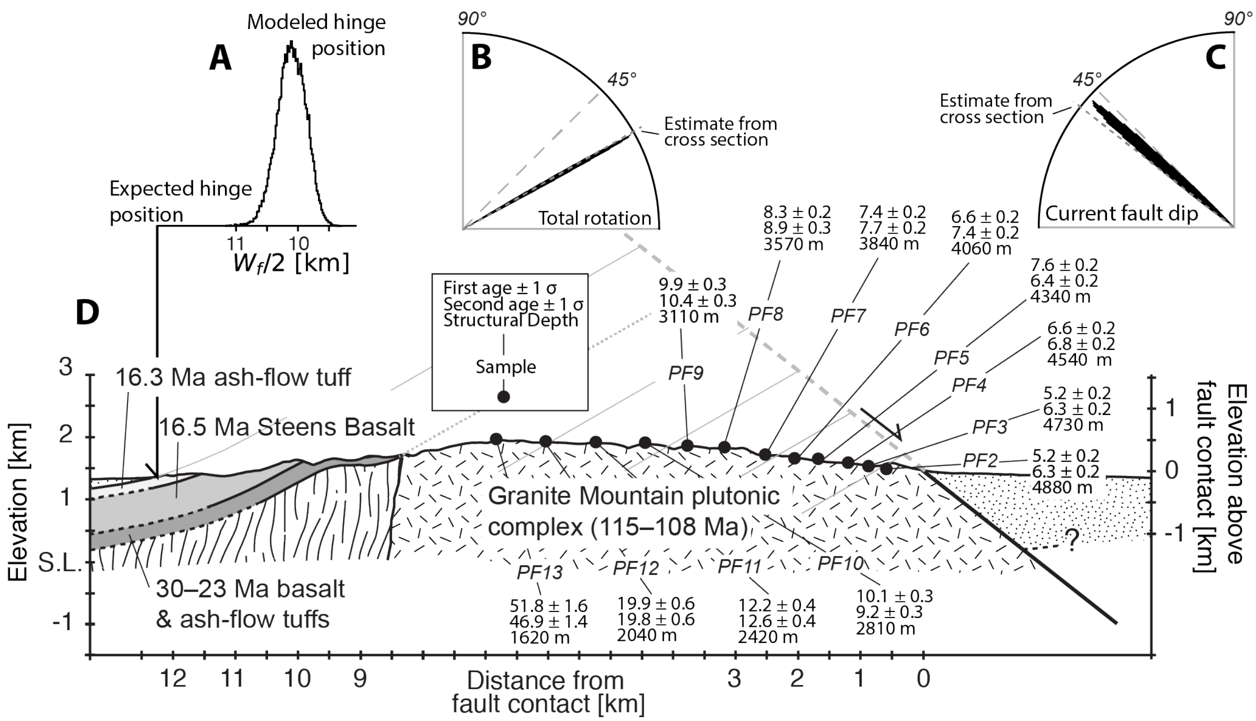

Figure 8. Simplified cross section of Pine Forest Range (**D**), adapted from Colgan, Dumitru, Reiners, et al., (2006), highlighting the sample locations and the two measured ages for each sample modelled with the simple rotation model. **A, B,** and **C** depict some of the geometric parameters of the fault block inferred from Markov chain Monte Carlo modeling of AHe ages, their current positions within the cross section (e.g. right axis and lower axis in **D**), and their structural depths. **A** highlights the distribution of modelled positions of the rotation axis (the expectation from Fig. 1 being that this would be located at the surface contact with pre-faulting sediments), **B** is a polar histogram of the amount of rotation, and **C** is the polar histogram of the current orientation of the fault.

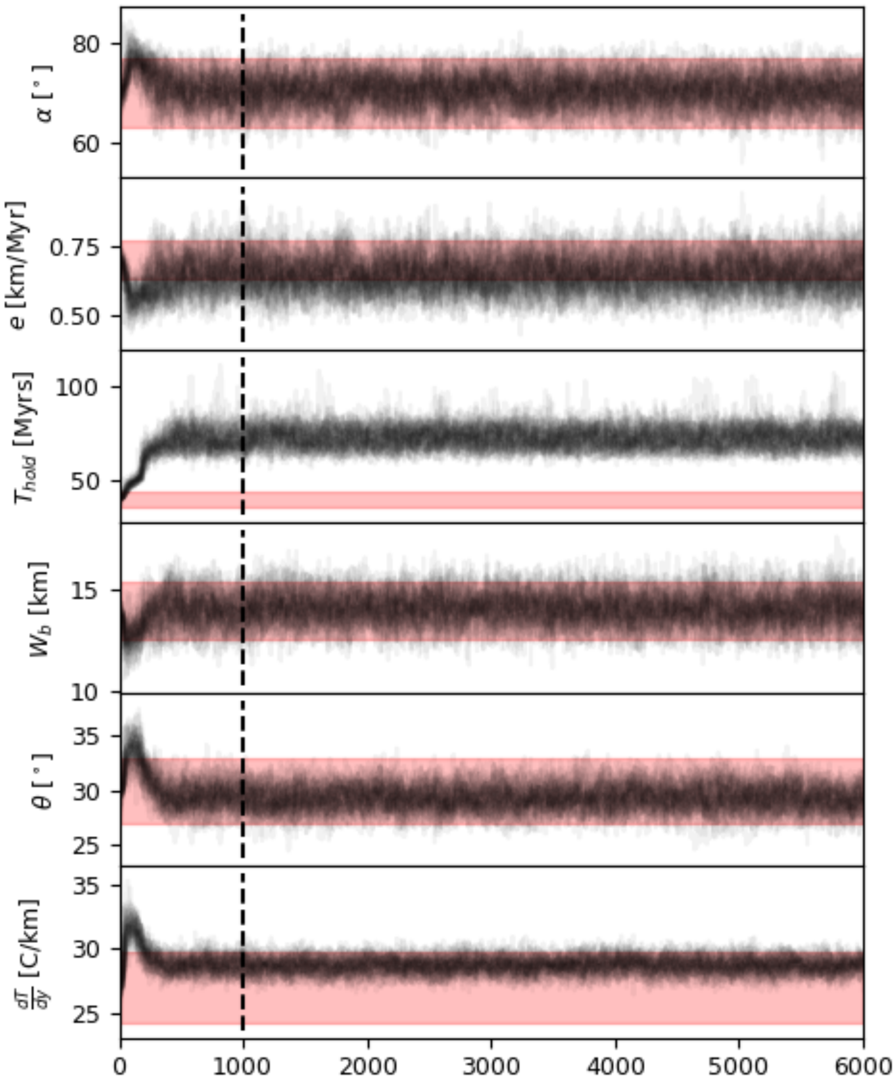

Figure 9. Plot of the sampled values of the Markov chain Monte Carlo Model for the Pine Forest Range as a function of the number of samples for each sampler. 40 grey, semi transparent lines in each plot represent each walker. Red Bar shows the 2σ bound of our initial guesses and vertical dashed line separates the burn-in period of the model from the collection phase.

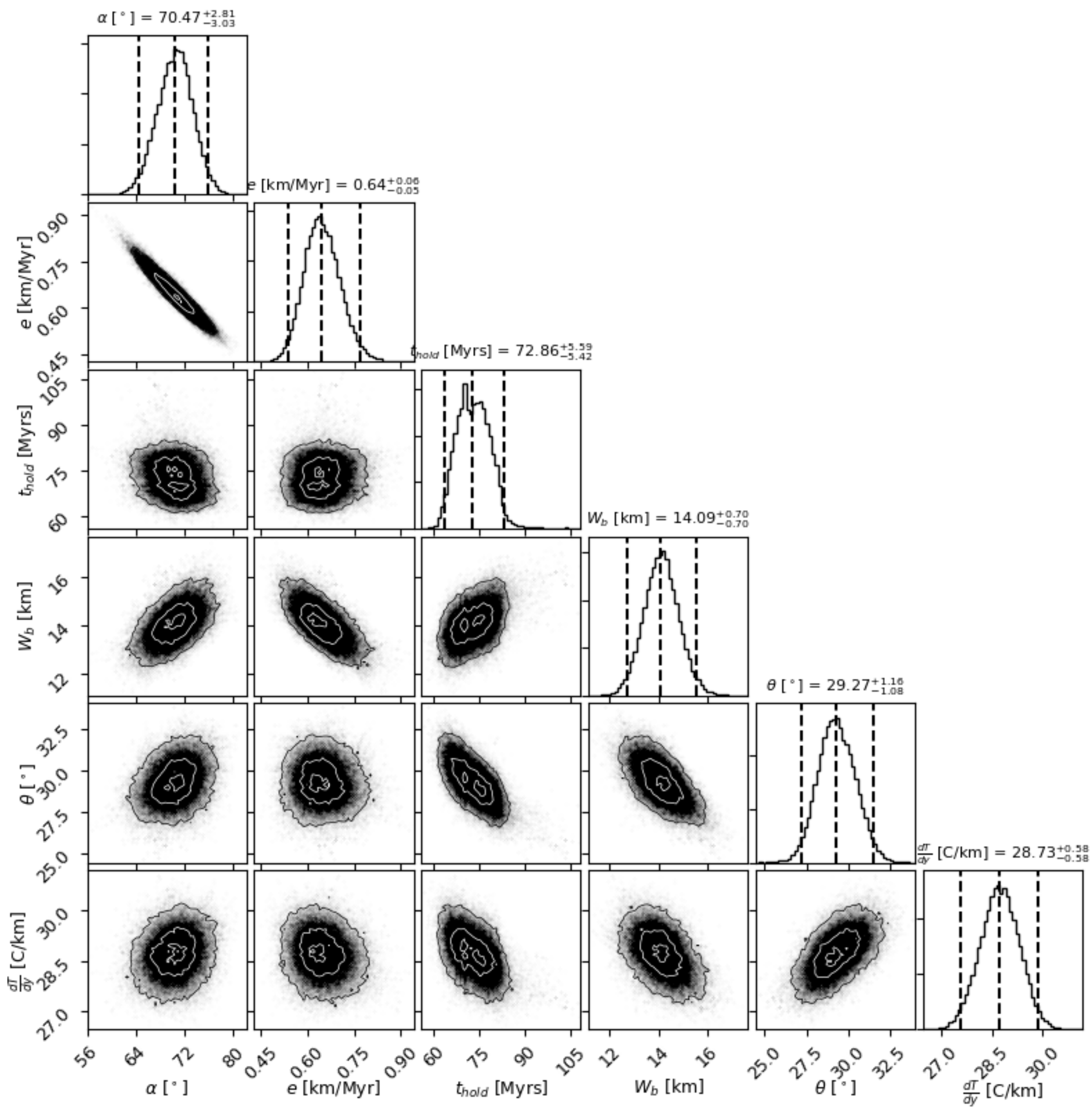

Figure 10. Corner plot highlighting the distributions of individual parameters for the Pine Forest Range revealed by the MCMC sampler and their covariance with one another. Upper diagonal row shows the histogram of sampled values and the 2.5th, 50th and 97.5th percentile of sampled values (also indicated in the titles). Contours in bivariate distributions surround 10%, 50%, and 95% of the samples.

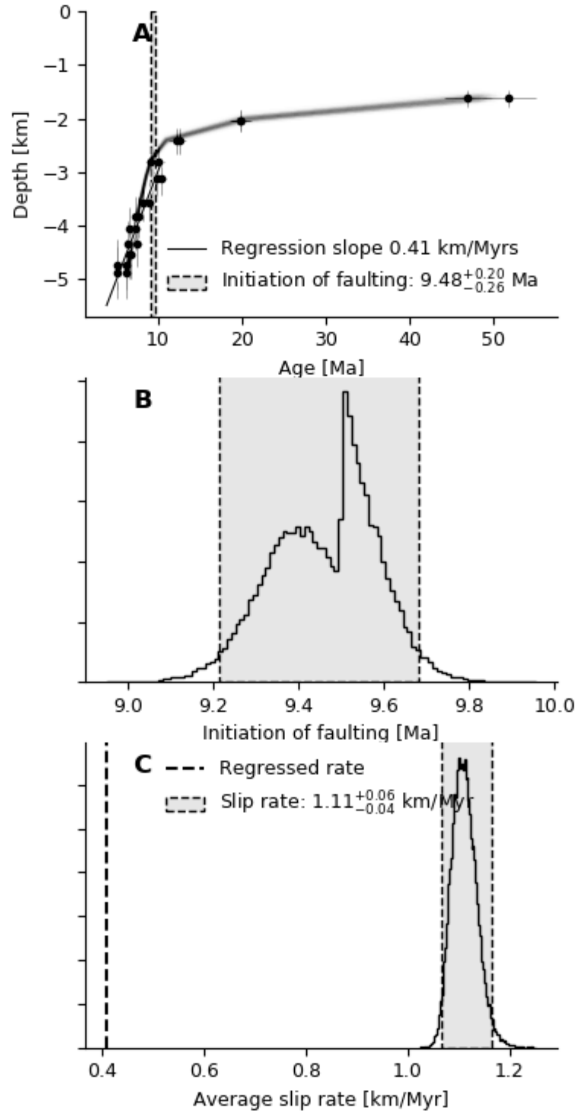

Figure 11. **A** plots observed (circles with 2σ error bars) and modelled age-depth relationships for the Pine Forest Range. Depth error is prescribed to be a 5% relative error. Modelled relationships are for a random selection of 250 model parameter sets from the MCMC chain. Thin, solid line highlights the regression of age-depth data (which excludes the oldest 3 samples, e.g. Colgan, Dumitru, Reiners, et al., 2006). Vertical bar is identical to **B**, highlighting the lower 2.5th percentile and upper 97.5th percentile of the predicted onset of faulting. **B** depicts the timing of the initiation of faulting, determined from the sampled parameter sets of the MCMC chain. **C** shows the distribution of average slip rates determined for the MCMC sampled parameter sets and the exhumation rate approximated from regressed data.

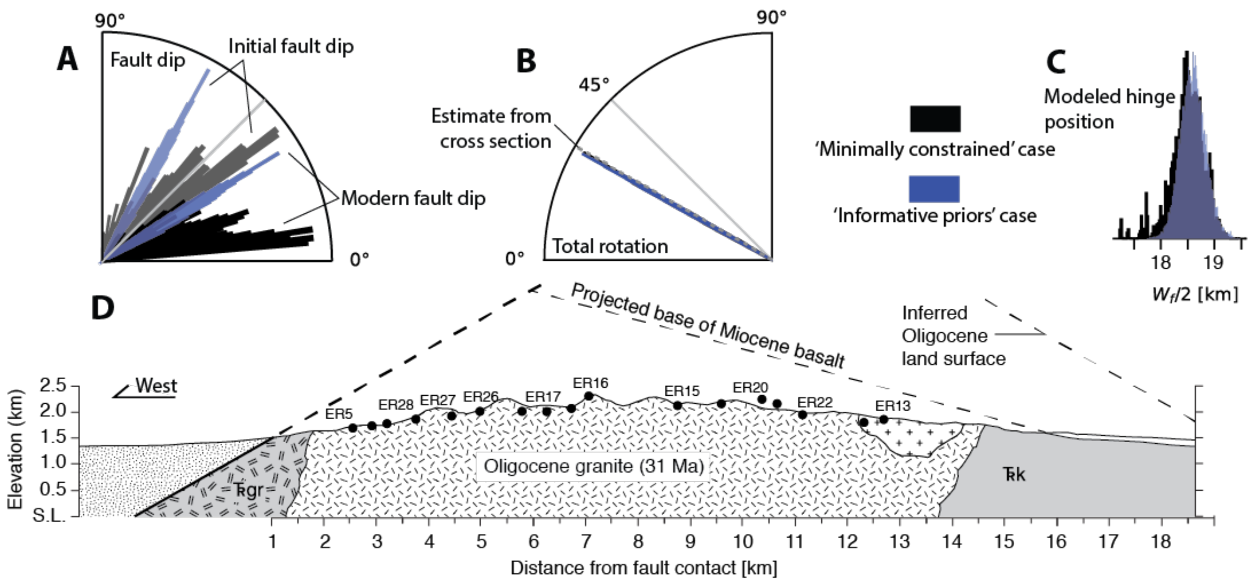

Figure 12. Simplified cross section of the East Range (**D**), adapted from (Fosdick & Colgan, 2008), highlighting the sample locations for each sample modelled with the simple rotation model (see Fig. 14 for ages). **A, B,** and **C** depict some of the geometric parameters of the fault block inferred from Markov chain Monte Carlo modeling of AHe ages, their current positions within the cross section, and their structural depths. Black and blue histograms show the results for two model configurations (see text for details). **A** is a polar histogram of the initial and current orientation of the fault, **B** is a polar histogram of the amount of rotation, and **C** highlights the distribution of modelled positions of the rotation axis.

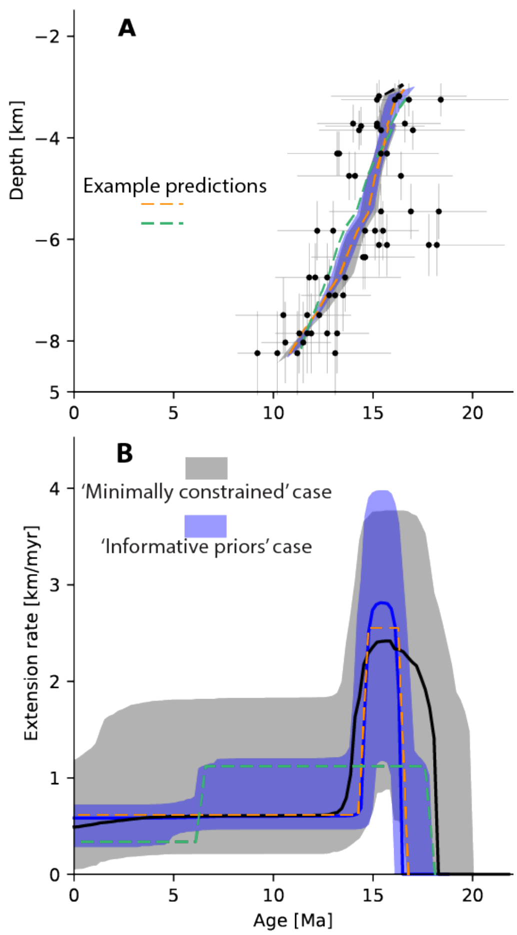

Figure 13. **A** plots observed (circles with 2σ error bars) and modelled age-depth relationships for the East Range. Shaded regions and central line are the upper 95th percentile and lower 5th percentile and median of modelled AHe ages and depths of 10,000 randomly drawn parameter sets from the posterior distributions of the minimally constrained (grey) and informative prior (blue) models. Orange and green lines show modelled age-depth relationships of the two special cases highlighted in Fig. 14. Depth error is prescribed to be a 5% relative error. **B** depicts the history of extension rates predicted by the same set of models.

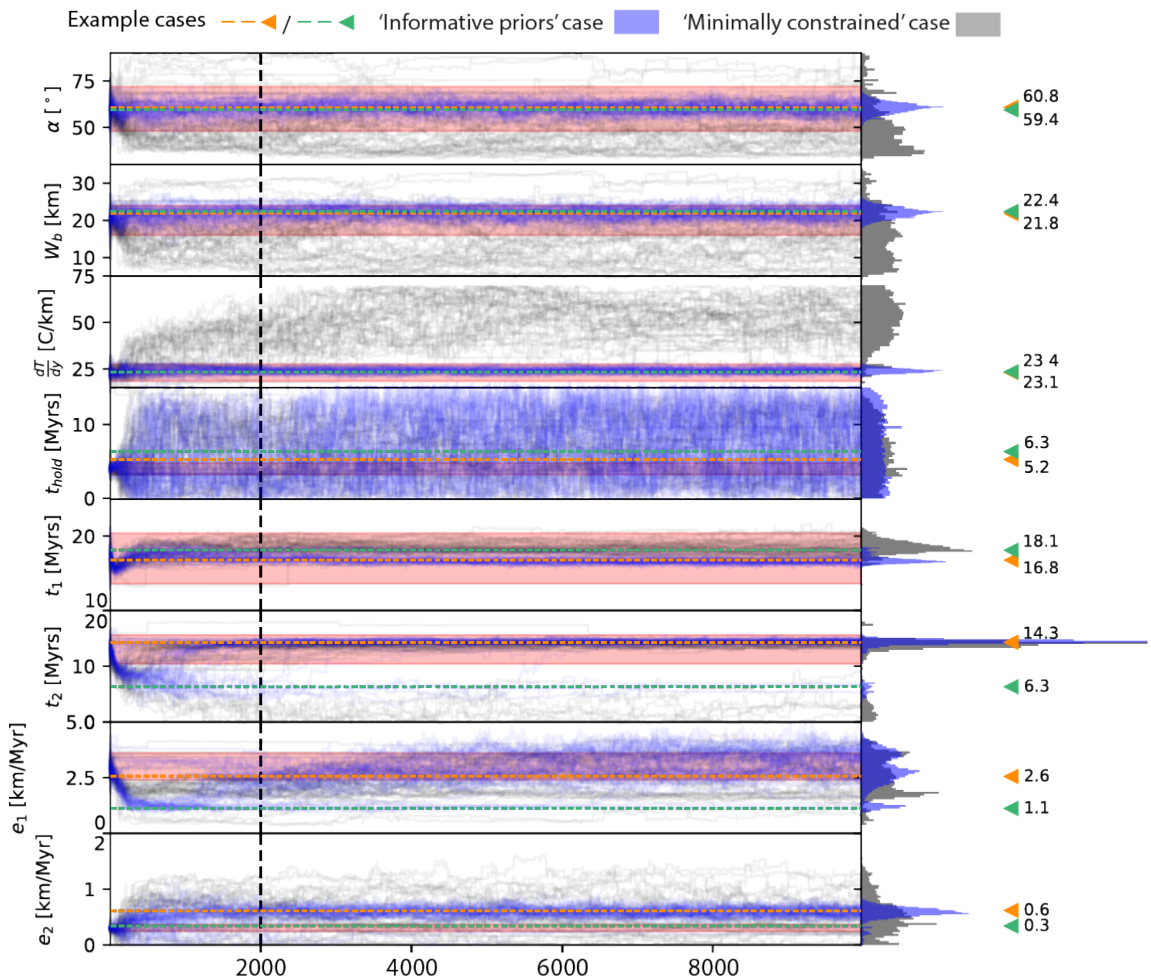

Figure 14. Plot of the sampled values of the Markov chain Monte Carlo Model for the East Range as a function of the number of steps for each walker. 40 semitransparent lines in each plot represent each walker, histograms on right axis approximate the posterior distribution (computed for the steps taken after the vertical dashed line). Grey lines and histogram are for the uninformative prior case, where values are limited to reasonable ranges. Blue lines and histograms assert Gaussian *prior* probabilities for the fault dip (60° ± 3°) and geothermal gradient (22 ± 1.6° C/km). Red Bar shows the 2σ bound of our initial guesses and vertical dashed line separates the burn-in period of the model from the collection phase. Orange and green lines and arrows indicate two special cases, with distinct histories of extension, identified by the modelled and plotted in Fig. 12 & 13.

Table 1. Table of base parameters for the 'narrow' fault block case about which individual parameters were varied to construct Fig. 6.

Parameter name, symbol	**Value [units]**
Extension rate, e	3 [km/Myr]
Rotation magnitude, θ	45 [°]
Fault block width, W_b	5 [km]
Initial fault angle, α	65 [°]
Erosion coefficient, k	0.4 [km/Myr]
Surface temperature, T_{surf}	10 [°C]
Geothermal gradient, dT/dZ	25 [°C/km]
Diffusivity, D	10^{-6} [m^2/s]

Table 2. Table of base parameters for the 'wide' fault block case about which individual parameters were varied to construct Fig. 7.

Parameter name, symbol	**Value [units]**
Extension rate, e	0.5 [km/Myr]
Rotation magnitude, θ	20 [°]
Fault block width, W_b	20 [km]
Initial fault angle, α	65 [°]
Erosion coefficient, k	1.5 [km/Myr]
Surface temperature, T_{surf}	10 [°C]
Geothermal gradient, dT/dZ	25 [°C/km]
Diffusivity, D	10^{-6} [m^2/s]